Ocean Engineering 280 (2023) 114944

Contents lists available at ScienceDirect

Ocean Engineering

journal homepage: www.elsevier.com/locate/oceaneng

Numerical study of aerodynamic performance of horizontal axis dual-rotor wind turbine under atmospheric boundary layers

Heming Bai [a], Nina Wang [b], Decheng Wan [a,*]

[a] Computational Marine Hydrodynamics Lab (CMHL), School of Naval Architecture, Ocean and Civil Engineering, Shanghai Jiao Tong University, Shanghai, China
[b] Key Laboratory of Far-shore Wind Power Technology of Zhejiang Province, Huadong Engineering Corporation Limited, Hangzhou, China

ARTICLE INFO

Handling Editor: Prof. A.I. Incecik

Keywords:
Horizontal axis dual-rotor wind turbine
Downstream wind turbines
Atmospheric boundary layer
Aerodynamic performance
Actuator line model
Large eddy simulation

ABSTRACT

The use of horizontal axis dual-rotor wind turbine (DRWT) is a new strategy to enhance the capture rate of wind energy and increase the performance of wind farms. An actuator line model (ALM) and large eddy simulation (LES) are introduced to investigate the aerodynamic performance of DRWT, and its effects on downstream turbines under convective atmospheric boundary layer (CBL) and neutral atmospheric boundary layer (NBL). The results conclude that the dominant vibration frequencies of the power production for the front rotor of DRWT are nearly the same as those of the single-rotor wind turbine (SRWT) under both NBL and CBL, but the vibration amplitude is slightly higher. The strength and dominant frequencies of yaw moment (Myaw) for the front rotor of DRWT are almost the same as those of the SRWT in both NBL and CBL flows, while the results of blade-root out-of-plane bending moment (Moop) are different. There are obvious differences in wake development and wake meandering between the DRWT and the SRWT. For three turbines cases, the total power production is increased respectively by 3.3% and 3% under NBL and CBL at a tandem spacing of 5D when the DRWT is placed in the first row, while the results increase to 5.5% and 4.4% at a tandem spacing of 9D. The stability of Myaw and Moop of second-row turbine located 5D downstream behind the DRWT under both NBL and CBL and Moop of all turbines located behind the DRWT in three tandem spacings (5D, 7D, 9D) under CBL are deteriorated compared with those located behind the SRWT.

1. Introduction

Environmental pollution has been aggravated by traditional fossil energy, and the promotion of renewable energy has become an effective way to improve the natural environment. Wind energy has advanced swiftly in the past few years due to its mature technology and easy development on a large scale. Over the next five years, the new offshore and onshore wind power generation capacity will be added over 469 GW (GWEC. GLOBAL, 2021). Wind energy is converted into mechanical energy of the turbine after the wind flow goes through the turbine. As a negative feedback to the flow field, a wake region with increased turbulent kinetic energy and decreased wind velocity will be formed behind the disk. The downstream turbines located in the wake region will be significantly affected, which will decrease the economic benefits of the wind farm (Sharma et al., 2018; Wu et al., 2019). Consequently, it is of great significance to study how to promote the performance of wind farms. Furthermore, when a turbine operates in atmospheric boundary layer (ABL), different atmospheric characteristics such as the wind shear, turbulent intensity, and thermal buoyancy affect the aerodynamic performance of the turbine (Churchfield et al., 2012) and its wake characteristics (Ning and Wan, 2019). Hence, the influence of ABL should be considered in the study of wind turbine aerodynamic performance.

The traditional method to improve the power production is to adjust the installation position of turbines to keep the downstream turbines away from the wake region, and this process is wind farm layout optimization. Analytical wake model (Katic et al., 1987; Larsen, 1988; Ainslie, 1988; Frandsen et al., 2006; Bastankhah and Porté-Agel, 2014) is applied to efficiently calculate the total power production and combine it with an optimization algorithm (mathematical programming (Gonzalez et al., 2013; Turner et al., 2014) or heuristic algorithms (Wan et al., 2012; Pookpunt and Ongsakul, 2013; Rehman and Ali, 2015; Hou et al., 2016)) to find the wind turbine arrangement with the maximum annual energy production (AEP) based on the local wind resources and wind farm constraints. The optimized wind farm arrangement allows downstream wind turbines to be staggered as much as possible from the

* Corresponding author.
E-mail address: dcwan@sjtu.edu.cn (D. Wan).

https://doi.org/10.1016/j.oceaneng.2023.114944
Received 5 October 2022; Received in revised form 24 March 2023; Accepted 24 May 2023
Available online 6 June 2023

wake region of upstream turbines in the prevailing wind direction. Nevertheless, in the remaining wind directions, the downstream turbines may still be fully affected. Consequently, the idea of "Vertically-staggered" was proposed by some scholars to further enhance the power production of wind farms (Wu et al., 2019; Chamorro et al., 2011, 2014; Vested et al., 2014; Zhang et al., 2019; Chatterjee and Peet, 2019). Meanwhile, this method was also applied to wind farm layout optimization (Chen et al., 2013; Chen et al., 2015; Vasel-Be-Hagh and Archer, 2017a). "Yaw angle control" is also an attempt to promote the performance of wind farms, it means that the rotor is no more perpendicular to the flow. Despite the performance of the yaw turbine will degrade, the downstream wake of the yaw turbine is skewed, thus more wind energy will be captured by the downstream wind turbines. This method has been extensively studied by many scholars, including wake characteristics (Howland et al., 2016; Marathe et al., 2016; Jiménez et al., 2009; Uemura et al., 2017), aerodynamic performance (Lee and Lee, 2019; Wang et al., 2019), applicability for large wind farms (Archer and Vasel-Be-Hagh, 2019) and yaw wake model (Bastankhah and Porté-Agel, 2016; Qian and Ishihara, 2018; Dou et al., 2019; Wei et al., 2021).

In recent years, to enhance the power production of wind farms, some relatively new methods have been propounded. For instance, counter-rotating wind turbine (CRWT) system and applying horizontal axis dual-rotor wind turbine (DRWT). The upstream and downstream wind turbine are rotated in opposite directions in the CRWT system, thus the downstream turbine can absorb more energy from the wake field of the upstream turbine. Yuan et al. (2014) investigated the effect of the CRWT system (contain two wind turbines) under neutral atmospheric boundary layer (NBL) based on wind-tunnel experiment, and it was concluded that the power production of the downstream turbine in CRWT system increased compared with co-rotating turbine system owing to the azimuthal velocity of the wake of the upstream turbine; however, the benefit of CRWT system declined gradually as the tandem spacing increases. Veisi et al. (Veisi and Shafiei Mayam, 2017) conducted a numerical investigation on similar problem based on large eddy simulation and obtained similar conclusions. According to the above researches, CRWT system is more suitable for situations where the tandem spacing between wind turbines is small, such as onshore wind farms with limited installation areas, while for offshore wind farms with large longitudinal spacing, its effect is limited. A new type of wind turbine that contains two rotors that are installed in close tandem spacing on the same tower is called horizontal axis dual-rotor wind turbine (DRWT) (Ozbay et al., 2014a). The "Betz limit" of this kind of wind turbine is higher than 59% (Newman, 1986), so its performance is dissimilar from the conventional horizontal axis single-rotor wind turbine (SRWT). Based on wind tunnel experiment, Ozbay et al. (2014b) investigated the aerodynamic performance of a DRWT with two same-size upwind rotors, and they concluded that the back-rotor of DRWT has a higher power production when two rotors rotating in opposite directions, and the total power production of DRWT is greater than that of SRWT. Wang et al., 2016a, 2018 and Hollands et al. (2020) also investigated the wake characteristics and aerodynamic performance of a DRWT with two differently-size upwind rotors based on wind tunnel experiment. Moghadassian et al., 2015, 2016 investigated the aerodynamic performance and wake characteristics of a DRWT with two differently-size upwind rotors based on the actuator line model (ALM) and LES under stable atmospheric boundary layer and NBL. The above researches focused on a single turbine, and the wake characteristics and aerodynamic performance of DRWT under different ABL flows are worth further study. Based on wind tunnel experiment, Wang et al., 2015, 2016b placed a SRWT behind a DRWT with two differently-size upwind rotors at different tandem spacings and investigated the performance of the downstream turbine, and they reported that the power output of the downstream turbine located behind the DRWT was less than that of the SRWT at a smaller longitudinal spacing. Vasel-Be-Hagh et al. (Vasel--Be-Hagh and Archer, 2017b) replaced all wind turbines in Lillgrund wind farm with DRWT with two same-size upwind rotors and calculated the power production for each row in NBL flow based on the ALM and LES, and an obvious increase in total power production was found compared with the Lillgrund wind farm containing only SRWT. However, the effects of DRWT on the aerodynamic loads of downstream turbines were not investigated in the above studies.

The use of DRWT is a new idea to promote the performance of wind farms, but research on this method is still limited. In this work, we first research the aerodynamic loads and wake characteristics of a DRWT working under different ABL with low surface roughness (represent sea-surface condition). Subsequently, to simplify the problem, we apply a DRWT to a three perfectly-aligned wind turbine group and arrange it to the first row to investigate its effects on downstream turbines in different ABL flows. The structure of DRWT refers to the work of Ozbay (Ozbay et al., 2014b) and Vasel-Be-Hagh (Vasel-Be-Hagh and Archer, 2017b), and NREL 5-MW wind turbine (Jonkman et al., 2009) is applied as a benchmark single-rotor design for SRWT and DRWT. The ALM is conducted to calculate the turbine aerodynamic performance.

Nomenclature

ALM	Actuator line model
ABL	Atmospheric boundary layer
CBL	Convective atmospheric boundary layer
DNS	Direct numerical simulation
DRWT	Dual-rotor wind turbine
LES	Large eddy simulation
Moop	Blade-root out-of-plane bending moment
Myaw	Yaw moment
NBL	Neutral atmospheric boundary layer
RANS	Reynolds-Averaged Navier-Stokes
RMS	Root mean square
SRWT	Single-rotor wind turbine
STD	Standard deviation

2. Materials and methods

2.1. Numerical method

2.1.1. Actuator line model

A large quantity of mesh is needed if a full-geometry wind turbine is used, thus reducing the computational efficiency. Therefore, we use actuator line model (ALM) proposed by Sørensen (Sørensen and Shen, 2002) to simplify the problem. Virtual lines are applied to replace all wind turbine blades in this method, and each line can be discretized into N blade elements, which is set to 40 in this work. The chord, blade airfoil type and aerodynamic parameters of each blade element are known, thus the blade can be replaced by the force vector parameterized according to the relative wind velocity and local 2D airfoil data.

$$f = (D, L) = \frac{1}{2}\rho U_{rel}^2 c dr (C_D \overrightarrow{e_D} + C_L \overrightarrow{e_L}) \tag{1}$$

In which D and L represent drag and lift forces at each blade element, respectively; c represents the local chord; ρ is air density; C_D and C_L denote the drag and lift coefficients, respectively; $\overrightarrow{e_D}$ and $\overrightarrow{e_L}$ respectively denote the unit vectors in the drag and lift directions; U_{rel} denotes the local velocity relative to the rotating blade computed by Eq. (2); dr denotes the width of the local element, and the geometric relationship between the local wind velocity, the local aerodynamic force and the angle of attack α is drawn in Fig. 1.

$$U_{rel} = \sqrt{U_z^2 + (\Omega r - U_\theta)^2} \tag{2}$$

Where U_θ and U_z are tangential and axial velocities of the inflow at blade elements, respectively; Ω denotes rotor rotation speed.

The vector force projection is done refer to Sørensen's (Sørensen and Shen, 2002) work, and the specific method is to project the concentrated vector force smoothly by a regularization function from a point to a

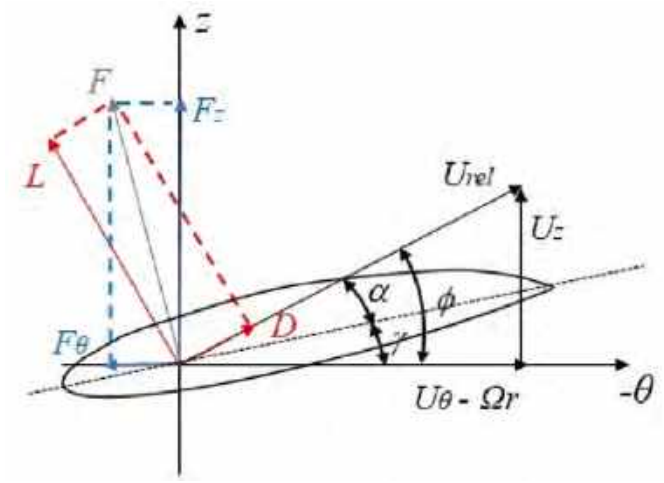

Fig. 1. Geometric relationship of vectors for the cross section of a blade element.

sphere-shaped area to avoid numerical errors, and then exert it onto the flow field. The regularization function is calculated as:

$$\eta_\varepsilon(d) = \frac{1}{\varepsilon^3 \pi^{\frac{3}{2}}} exp\left[-\left(\frac{d}{\varepsilon}\right)^2\right] \tag{3}$$

The radius of the sphere-shaped area is calculated as:

$$R_{sphere} = \varepsilon\sqrt{3\ log_e 10} \tag{4}$$

The smooth aerodynamic force generated by all blade elements at (x, y, z, t) is calculated as:

$$f_\varepsilon = f \otimes \eta_\varepsilon = \sum_{i=1}^{N} f_i(x_i, y_i, z_i, t) \frac{1}{\varepsilon^3 \pi^{3/2}} exp\left[-\left(\frac{d_i}{\varepsilon}\right)^2\right] \tag{5}$$

In which N represents the number of blade elements; (x_i, y_i, z_i) denotes the coordinate of a certain blade element; d_i represents the distance between the location of *ith* blade element and a certain grid point (x,y,z); ε denotes a constant parameter uses to adjust the regularization function, and it is better to keep $\varepsilon = 2\Delta x$, twice of the grid size near the blade, refering to the work of Troldborg et al. (2009) to ensure the stability of numerical simulation (Fig. 2).

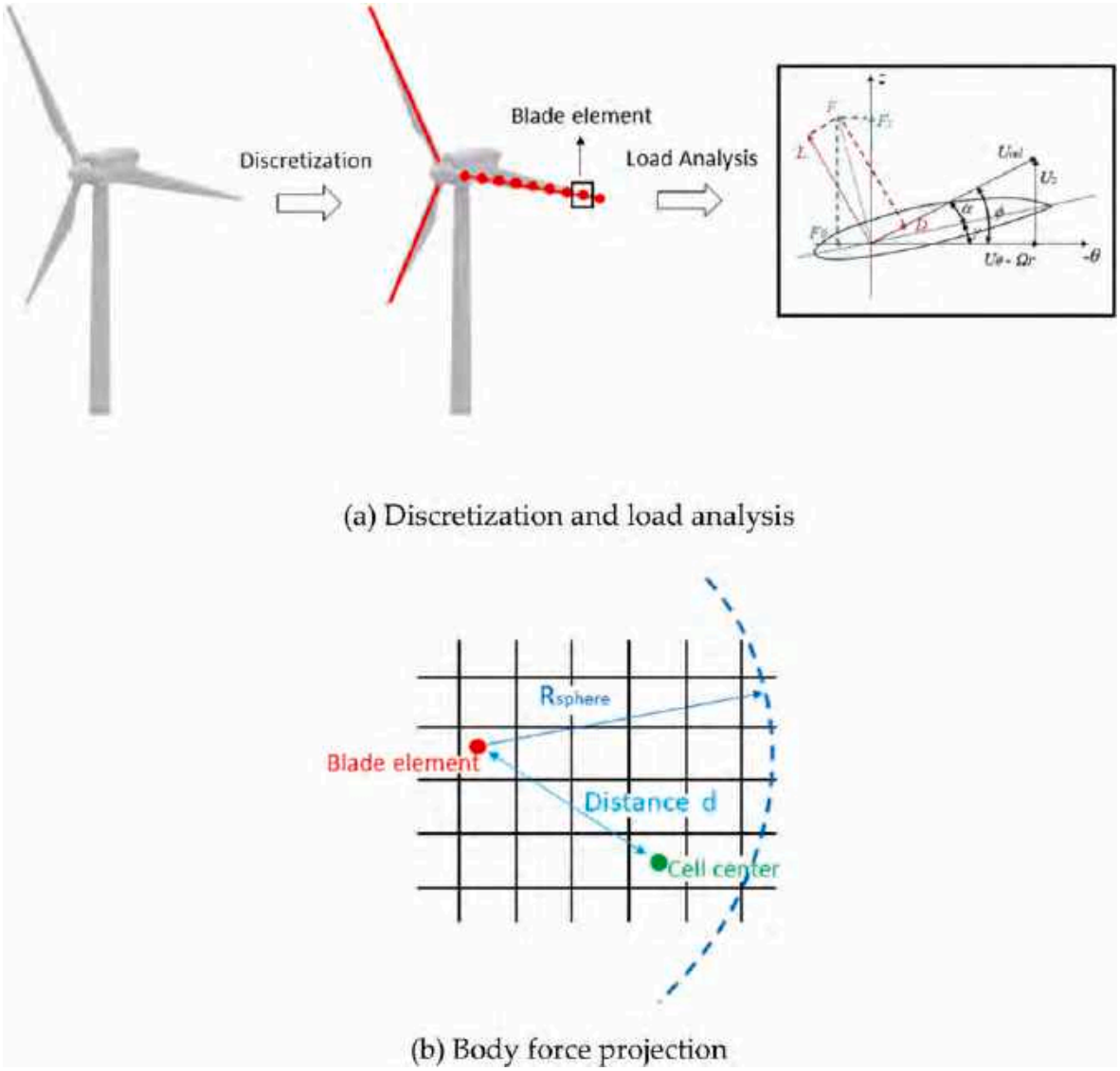

Fig. 2. Basic diagram of actuator line model.

2.1.2. Governing equations

Wind turbine wake under ABL is a high Reynolds number turbulent flow governed by N-S equations with a wide range of time and length scales, and there are three well-known approaches to resolve the turbulence (Zhong et al., 2015). Reynolds-Averaged Navier-Stokes (RANS) method cannot capture the flow field details due to the time-averaged treatment of physical quantities; in contrast, Direct numerical simulation (DNS) method can resolve the full-scales turbulence eddies, but it requires high temporal and spatial resolution and consumes a large amount of computational expenditure, thus it is not suitable for complex flow in engineering problems. Large eddy simulation (LES) method is a compromise between RANS and DNS. It directly solves large-scale eddy larger than the filter scale and a subgrid-scale (SGS) model is applied to modeled the subgrid-scale stress. LES has shown excellent performance in numerical computation problems in the field of wind turbine (Lu and Porté-Agel, 2011; Fleming et al., 2014; Abkar and Porté-Agel, 2015; Allaerts and Meyers, 2015; Tian et al., 2020).

The filtered governing equations are shown below:

$$\frac{\partial \widetilde{u}_i}{\partial x_i} = 0 \tag{6}$$

$$\frac{\partial \widetilde{u}_i}{\partial t} + \widetilde{u}_j \frac{\partial}{\partial x_j}(\widetilde{u}_i) = \underbrace{-\frac{\partial \widehat{p}}{\partial x_i}}_{I} \underbrace{-\frac{1}{\rho_0}\frac{\partial}{\partial x_i}\widetilde{p_0}(x,y)}_{II} \underbrace{-2\varepsilon_{i3k}\Omega_3\widetilde{u}_k}_{III} \underbrace{+g\left(\frac{\widetilde{\theta}-\theta_0}{\theta_0}\right)\delta_{i3}}_{IV} + \underbrace{\frac{1}{\rho_0}f_i^T}_{V} \underbrace{-\frac{\partial}{\partial x_j}\left(\tau_{ij}^D\right)}_{VI} \tag{7}$$

$$\frac{\partial \widetilde{\theta}}{\partial t} + \widetilde{u}_j \frac{\partial \widetilde{\theta}}{\partial x_j} = -\frac{\partial q_j}{\partial x_j} \tag{8}$$

where "~" donates a spatial filtering of the grid scale $\widetilde{\Delta}$; $\widetilde{u}_j = u_j - u_j'$ represents the resolved-scale velocity, and the u_j' is the SGS velocity vector; $\widetilde{\theta}$ is the resolved-scale potential temperature. In Eq. (7), term I represents the gradient of the modified pressure $\widehat{p}$, including two parts—resolved-scaled pressure normalized by density together with one-third of the trace of the stress tensor, $\tau_{kk}/3$. Term II denotes imposed background pressure gradient, which is used as one of external forces to drive the generation of ABL. Term III represents the Coriolis force induced by the rotation of the earth, in which ε_{i3k} and $\Omega_3 = \omega[0, cos\,\varphi, sin\,\varphi]$ are the alternating tensor and the rotation rate vector, respectively, where ω denotes the planetary rotation rate and φ represents the latitude. Term IV represents the buoyancy effects calculated by the Boussinesq approximation, in which θ_0 denotes the reference temperature, and it is taken to be 300K. The body force generated by the blades in term V is modeled by ALM in section 2.1.1. Term VI is the divergence of the fluid stress tensor including viscous and subgrid effect, and it can be shown as follow:

$$\tau_{ij}^D = \tau_{ij} - \frac{\delta_{ij}\tau_{kk}}{3} = -2v^{SGS}\widetilde{S}_{ij} \tag{9}$$

$$\widetilde{S}_{ij} = \frac{1}{2}\left(\frac{\partial \widetilde{u}_i}{\partial x_j} + \frac{\partial \widetilde{u}_j}{\partial x_i}\right) \tag{10}$$

$\widetilde{S}_{ij}$ is the resolved strain-rate tensor. δ_{ij} is Kronecker delta. v^{SGS} represents SGS eddy viscosity and is calculated as:

$$v^{SGS} = (C_s\Delta)^2\left(2\widetilde{S}_{ij}\widetilde{S}_{ij}\right)^{1/2} \tag{11}$$

where C_s is Smagorinsky coefficient and it is set to 0.13 (Churchfield et al., 2012). $\Delta = (\Delta x \Delta y \Delta z)^{1/3}$ denotes the filter length scale.

q_j in Eq. (8) denotes the temperature flux and it can be modeled completely considering the SGS effect as:

$$q_j = -\frac{v^{SGS}}{Pr_t}\frac{\partial \widetilde{\theta}}{\partial x_j} \tag{12}$$

In which Pr_t donotes the turbulent Prantdl number, and it is set to 1/3 in both NBL and CBL flows (Churchfield et al., 2012).

2.2. Computational Setup

Precursor-successor simulation is used to generated the ABL inflow which satisfy turbulent multi-scale characteristics. This method is combined with actuator model to form an open source solver "SOWFA" which is developed by NREL (Churchfield and Lee, 2013). This solver has been widely applied to numerical simulation of wind turbine aerodynamic performance under ABL (Churchfield et al., 2012; Ning and Wan, 2019; Fleming et al., 2014; Tian et al., 2020; Zheng et al., 2018). In this work, we adapt the SOWFA and refer to the above literature in the process of parameter setting.

2.2.1. Precursor simulation

The main idea of precursor simulation is to artificially apply external forces to drive the flow field from an initial laminar shear flow to a fully developed turbulent boundary layer flow containing multi-scale turbulent vortices (Ning and Wan, 2019). The wall model of Moeng (1984) is applied to simulate the temperature flux and surface stress at the lower boundary, and we set the surface roughness height z_0 to 0.001 to represent the offshore conditions; the average surface temperature flux q_s are respectively set as $0.00\text{K} \bullet \text{m/s}$ and $-0.04\text{K} \bullet \text{m/s}$ for NBL and CBL; the friction velocity u_* can be simulated based on the Monin-Obukhov similarity theory. To guarantee the flow field is fully developed, a long computational domain is required, so four vertical boundaries of the computational domain are set to cyclic boundary conditions in order to save computational expenditure. The upper boundary is set to slip condition, which means that the vertical velocity gradient and flux are set to zero. The size of the domain is set as 3000m × 3000m × 1000m in the length, width and height directions, respectively. A uniform orthogonal mesh grid of a grid number of 300 × 300 × 100 is used in the length, width and height directions with the grid size of 10m. Furthermore, in order to avoid the horizontal velocity and the turbulent structure being stuck, we set the wind direction to be from 240° (Southwest) (Churchfield et al., 2012). Fig. 3 shown the computational domain and boundary conditions in the precursor simulation.

The average wind speed is set to the rated speed $U_{hub} = 11.4\text{m/s}$ in the hub height plane. From the lower surface to 700m in vertical di-

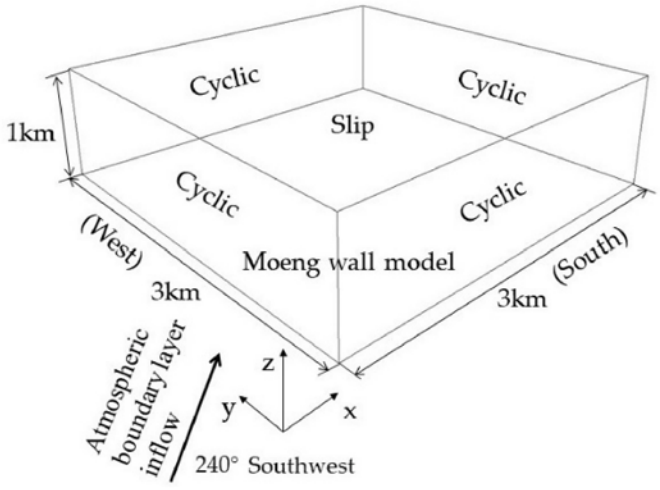

Fig. 3. Computational domain and boundary conditions in the precursor simulation.

rection, the potential temperature is set to 300K, and it increases linearly to 308K from 700 to 800m, which is known as capping inversion region. The last 200m, the potential temperature grows at a rate of 0.003K/ m. To guarantee the flow field is fully developed in the precursor simulation stage, the computation lasts 18000s for both NBL and CBL cases, and the time step is set as 0.4s.

84 CPU cores were used for precursor simulation, and the computation time is about 10 days.

2.2.2. Successor simulation

Successor simulation refers to the numerical calculation of wind turbine aerodynamic performance in ABL flow. Based on the background mesh used in the precursor simulation stage, two refinement processes (RegionII—5m and Region III—2.5m) are adopted in this work with the aim of finely capturing the flow details near the turbine and in the wake region. The grid number is approximately 26 million. At this stage, the upstream vertical boundary uses the quasi-equilibrium state ABL inflow data saved from the precursor simulation at each time-step, while the downstream vertical boundary are modified from cyclic boundary conditions to zero-gradient boundary conditions. Fig. 4 draws the details of the computational domain and the turbine layout.

Successor simulation run continuously up to 1300s for all cases to ensure the wind adequately flows through the turbines in the computational domain. The time step should satisfy the CFL condition (Eq. (13)) to guarantee numerical stability.

$$max\left\{\left|\frac{U\Delta t}{\Delta x}\right|,\left|\frac{\Omega R\Delta t}{\Delta x}\right|\right\} < 1 \tag{13}$$

In which $U = 11.4\mathrm{m/s}$ represents average inflow wind speed in the hub height plane; Ω is the rotation speed of the rotor; R denotes the radius of rotor; $\Omega R = (12.1 \times 2\pi \times 63)/60 \approx 80m/s$ represents the tangential velocity at the edge of the rotor, and it is much larger than U, thus, $\Delta t < |\Delta x/\Omega R| = |2.5/80| \approx 0.031s$, so the time step is set as 0.02s.

We set WT1 to DRWT or SRWT, and both WT2 and WT3 are set to conventional SRWT. The longitudinal spacing Δx between two adjacent turbines is set as 5D, 7D and 9D (D represents the rotor diameter). Considering the work of Ozbay et al. (2014b), counter-rotating configurations of DRWT can generate more power compared with co-rotating configurations, thus we adopt the counter-rotating configurations. Besides, the longitudinal spacing between the front and back rotor of DRWT is set to 0.25D (Ozbay et al., 2014b). Fig. 5 shows two kinds of turbine layout and Table 1 lists the calculation cases.

In this work, NREL 5 MW wind turbine (Jonkman et al., 2009) is used as the benchmark single-rotor design for both SRWT and DRWT, and Table 2 lists the gross parameters.

84 CPU cores were used for successor simulation, and the computation time of each case is about 12 days.

3. Results and discussions

In this section, the characteristics of two types of ABL flows and ALM are verified in the first part; subsequently, the aerodynamic performance and the wake characteristics of a SRWT and DRWT are compared and analyzed under two kinds of ABL; in the last part, the cases contain three wind turbines arranged in tandem in two types of ABL are calculated and analyzed. The wind field data of the last 600s out of 1300s is used in this work.

3.1. Validation of ABL characteristics and ALM

The ABL flow field is complex, and the spatial scale of the turbulent vortices can span from a few millimeters to several kilometers. Large-scale turbulent vortices can derive energy from the Reynolds stress work of the mean flow as well as the thermal buoyancy work, and the energy will be transferred to meso- and small-scale turbulent vortices and finally dissipated in the minimum-scale turbulent vortices. The power spectrum of streamwise and vertical fluctuation velocities at hub height under ABL based on precursor simulation are shown in Fig. 6, in which the vertical axis and horizontal axis respectively denote dimensionless power spectral density of velocity fluctuation ($Su'/(Du_{hub})$ and $Sw'/(Du_{hub})$) and frequency f. Red solid line and blue dash line respectively represent CBL case and NBL case, and the black solid line denotes "-5/3 power law".

From Fig. 6, it is clearly found that the large-scale turbulent vortices at low frequency region have greater turbulence energy; the streamwise and vertical fluctuation velocities both decrease as the frequency increases, and the trend satisfies the "-5/3 power law", which means that the atmospheric turbulent based on precursor simulation satisfies the energy cascade theory. In addition, the CBL case contains more fluctuation velocity energy in the frequency domain due to the stronger thermal buoyancy, and this phenomenon can be directly visualized by the contours of fluctuation velocity under two types of ABL in Fig. 7.

The time-averaged streamwise velocity profiles non-dimensionalized

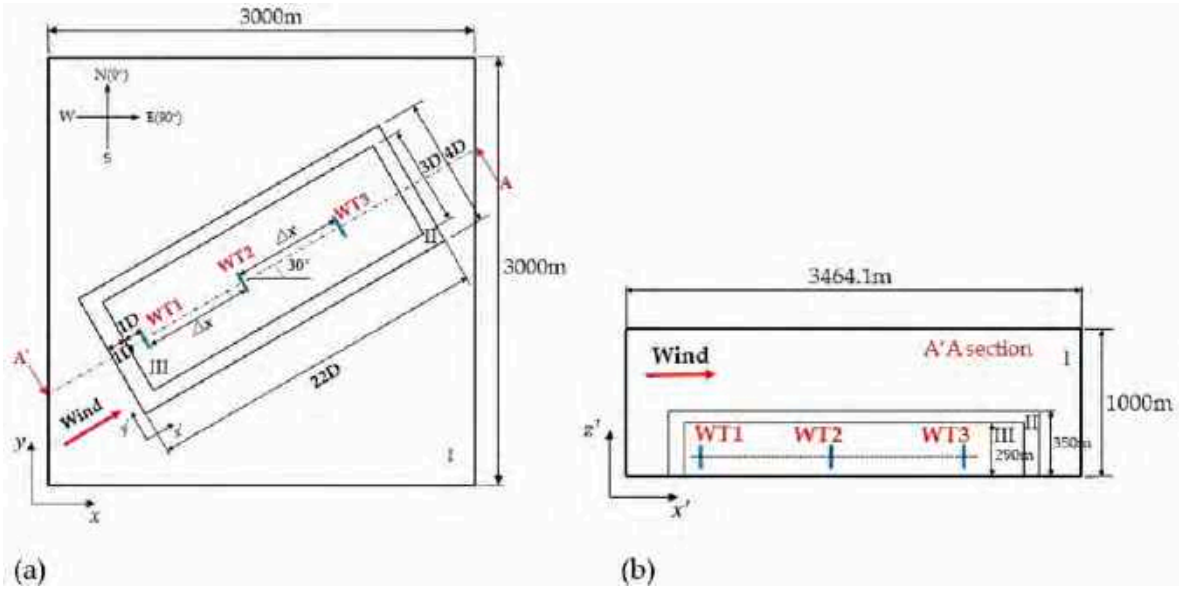

Fig. 4. Computation domain. (a) Horizontal plane; (b) Central longitudinal plane.

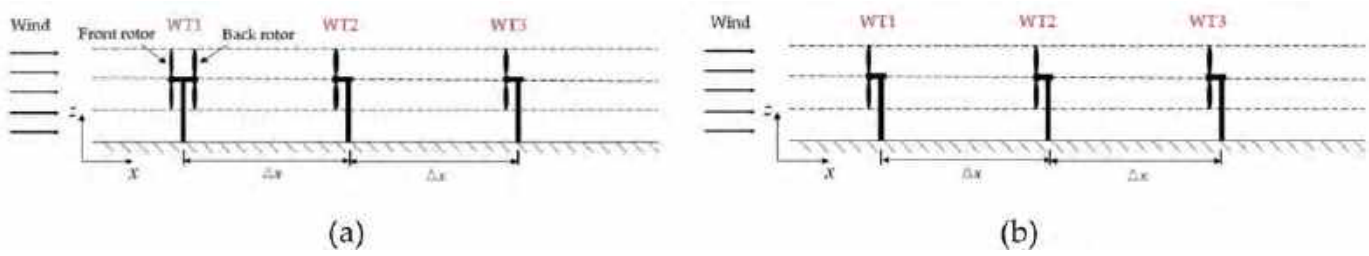

Fig. 5. Wind turbine group layout. (a) DRWT; (b) SRWT.

Table 1
Overview of the calculation cases.

Case	$\triangle x$	WT1	Stability of ABL	Number of Turbines
1	–	SRWT	Neutral	1
2	–	DRWT	Neutral	1
3	–	SRWT	Convective	1
4	–	DRWT	Convective	1
5	5D	SRWT	Neutral	3
6	5D	DRWT	Neutral	3
7	5D	SRWT	Convective	3
8	5D	DRWT	Convective	3
9	7D	SRWT	Neutral	3
10	7D	DRWT	Neutral	3
11	7D	SRWT	Convective	3
12	7D	DRWT	Convective	3
13	9D	SRWT	Neutral	3
14	9D	DRWT	Neutral	3
15	9D	SRWT	Convective	3
16	9D	DRWT	Convective	3

Table 2
Gross parameters of NREL 5 MW wind turbine.

Item	Value
Rating	5 MW
Hub height	90m
Rotor diameter	126m
Rated wind speed	11.4 m/s
Rotor configuration	3 Blades
Rated rotation speed	12.1 rpm
Rotor orientation	Upwind

by $U_{hub} = 11.4\text{m/s}$ along the vertical direction under two kinds of ABL are shown in Fig. 8(a), and the height of the bottom, the hub and the top of the rotor of the NREL 5 MW wind turbine are represented by the three horizontal dash lines, respectively. It is clearly shown that the wind velocity satisfies the initial setting. The wind shear flow stratification is disturbed by the vertical thermal buoyancy in CBL case, thus the vertical gradient of streamwise wind velocity is lower than NBL case. The wind velocity distribution near the ground (approximately less than 100m) in NBL flow is subject to the logarithmic law (Emeis, 2018), and the streamwise velocity distribution in NBL flow and the fitted logarithmic profile are drawn in Fig. 8(b) in the semi-logarithmic coordinate system. It is found that the velocity distribution satisfies the "logarithmic law" well in the near ground region ($z/z_{hub} < 1.1$, where z_{hub} denotes the hub height of NREL 5 MW wind turbine).

The setting of the potential temperature along the z-direction in the precursor simulation stage is described in section 2.2.1. The time-averaged potential temperature profile of the fully developed wind field under two types of ABL is shown in Fig. 9. It is found that the potential temperature satisfies the initial setting under NBL, and higher potential temperature below 700m is found in the CBL case due to the temperature flux.

The time variation curves of power output at $U_{hub} = 11.4\text{m/s}$ under two kinds of ABL are shown in Fig. 10. The blue and red solid lines represent the time history curve of power output and time-averaged power, respectively. It is found that the power output fluctuates with time due to the disturbance of atmospheric turbulence, while the time-averaged power output is around 5 MW under two types of ABL, indicating that the aerodynamic loads of the turbine can be accurately estimated by ALM.

Based on above analysis and discussion, it can be proved that the precursor-successor simulation together with ALM can accurately simulate the flow field characteristics of ABL and the aerodynamic performance of the turbine.

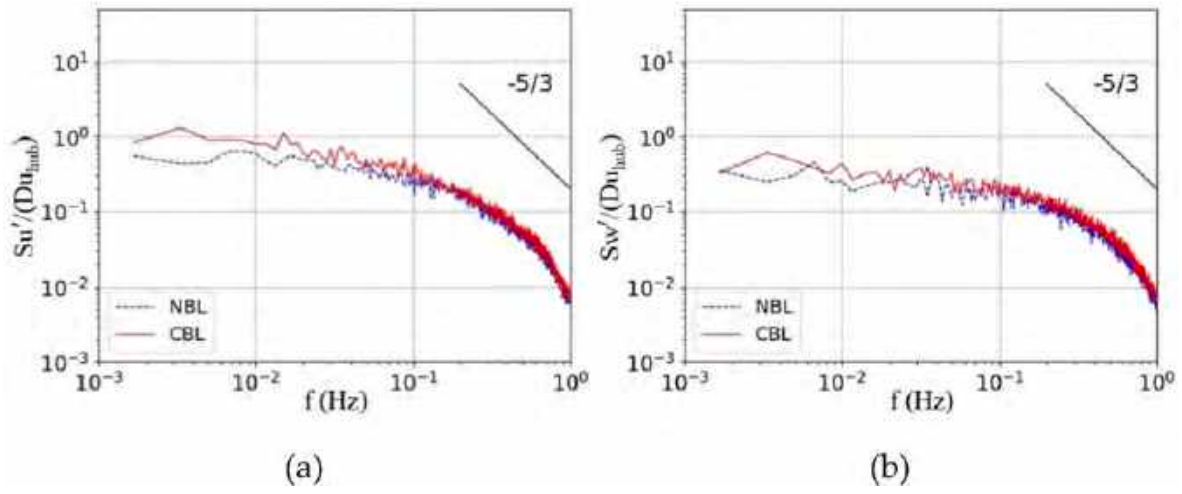

Fig. 6. Power spectrum of fluctuation velocity at hub height under ABL. (a) Streamwise fluctuation velocity; (b) Vertical fluctuation velocity.

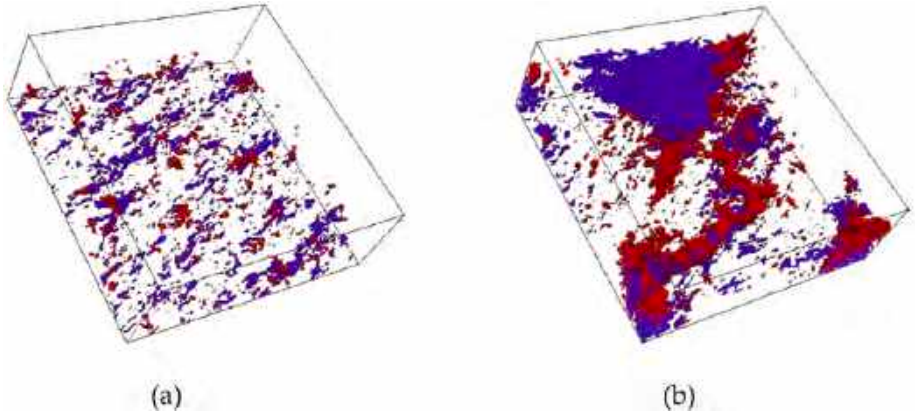

Fig. 7. Contours of vertical (red, 0.8 m/s) and streamwise (blue, −1.2 m/s) fluctuation velocities under ABL. (a) NBL; (b) CBL.

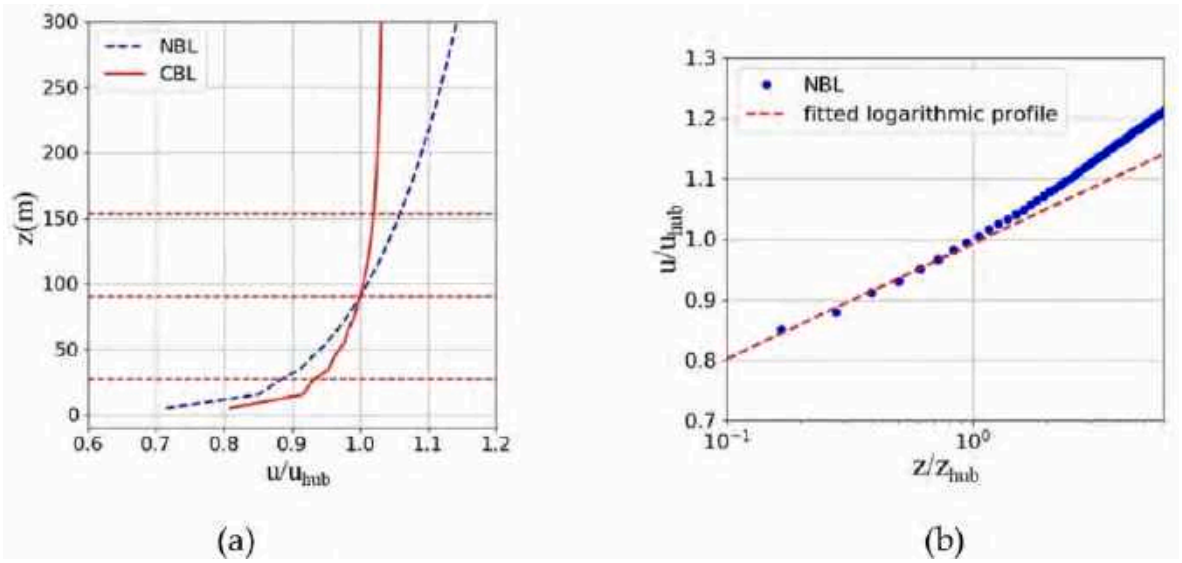

Fig. 8. Time-averaged streamwise wind velocity profile. (a) Comparison of two types of ABL flows; (b) Wind velocity profile on a semi-logarithmic coordinate system under NBL.

3.2. Aerodynamic performance and wake characteristics of DRWT under ABL

In this section, the power production, aerodynamic moments, and wake characteristics of the SRWT and DRWT are compared and analyzed under two types of ABL.

3.2.1. Analysis of power production

The time-averaged power production of the SRWT and the DRWT under two types of ABL are shown in Fig. 11. Since the power production is influenced by the average wind speed on the rotor, which is almost the same in NBL and CBL flows (as shown in Fig. 8), thus different ABL flows have little effect on the time-averaged power production of a single turbine.

The power production of the front rotor of DRWT is reduced compared with that of the SRWT, and this is because the back rotor of DRWT affects the performance of the front rotor. Fig. 12 shows the time-averaged attack angle profiles along the blade radius of SRWT and the front rotor of DRWT in NBL and CBL flows. It is clearly found that the attack angle of the front rotor of DRWT is smaller than that of SRWT. However, there is almost no difference between the time-averaged attack angle along the blade radius in NBL and CBL flows. Moreover, the total power production of the DRWT is larger than that of the SRWT, which agree with the results of Obzay et al. (Ozbay et al., 2014b), and it reveals the advantage of DRWT in power production.

The spectrum of power output can reveal the vibration characteristics and the dominant vibration frequencies of power output, and it can be obtained by the Fast Fourier Transform (FFT) of the power output time-history sequence. Fig. 13 shows the spectrum of power output for SRWT and DRWT in NBL and CBL flows, and the five scatter points in the figure correspond to the dominant frequencies of the highest power vibration amplitude for SRWT and DRWT. The frequency in x-axis is nondimensionalized by $St = fD/u_{hub}$. It is found that the main vibration frequencies of the power are in the low-frequency region, and the vibration amplitude is more severe in the case of CBL in this region since the low-frequency large-scale turbulence has more energy and it is higher in the case of CBL, which conforms to the results of Fig. 6. The main vibration frequencies of the power for the front rotor of DRWT are almost the same as that of the SRWT, while the vibration amplitude of the front rotor is slightly higher than that of the SRWT, suggesting that the influence of the back rotor on the power output of the front rotor is only reflected in the vibration amplitude. The spectrum of power output for both SRWT and the front rotor of DRWT have peaks at the position of the "Blade passage frequency" (as shown by the black dash line in Fig. 13, $St = 6.69$), because NREL 5 MW wind turbine contains three blades, which sweep the complete disk area of the turbine every 1/3

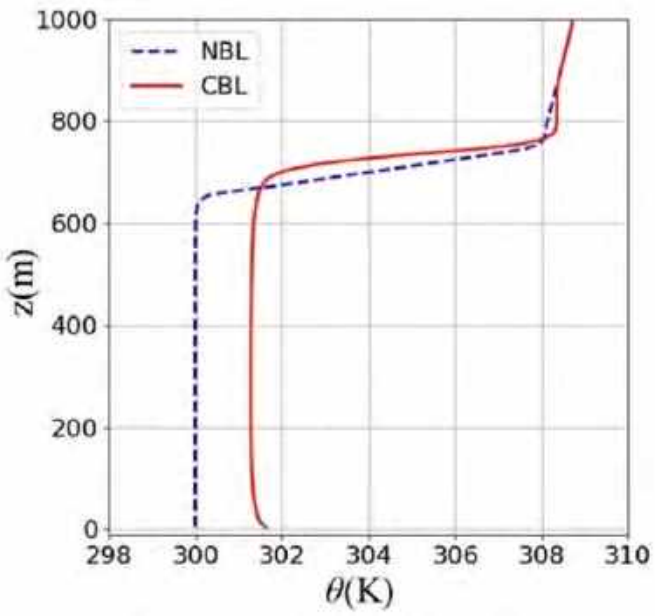

Fig. 9. Time-averaged potential temperature profile.

rotation period with a significant power vibration; however, vibration caused by spatial location change is smaller than the effects of large-scale turbulence. The rotation speed of the back rotor decreases due to the absorption of inflow wind energy by the front rotor, thus the "Blade passage frequency" of the back rotor is smaller than that of the front rotor.

3.2.2. Analysis of aerodynamic moments

The yaw moment (M_{yaw}) and blade-root out-of-plane bending moment (M_{oop}) are calculated in this work, and the specific expressions are shown in Eq. (14) and Eq. (15):

$$M_{yaw} = \sum_{j=1}^{N_b} \sum_{i=1}^{N_r} \left(\vec{r}_{i,j} \times \vec{F}_{i,j} \right) \cdot \vec{e}_t \tag{14}$$

$$M_{oop} = \sum_{i=1}^{N_r} \left(\vec{r}_{i,j} \times \vec{F}_{i,j} \right) \cdot \vec{e}_{\theta,j} \tag{15}$$

In which N_r represents the total number of the radial elements of one blade, N_b denotes the total number of blades, j refers to each blade, i represents different discrete radial blade elements, $\vec{F}_{i,j}$ denotes the aerodynamic force vector at the *ith* radial blade element on the *jth* blade, $\vec{r}_{i,j}$ represents the distance vector between the *ith* radial blade element on the *jth* blade and the apex of all blades. $\vec{e}_{\theta,j}$ and $\vec{e}_t$ represent the tangential unit vector along the circumferential rotation on the *jth* blade at circumferential position θ and the unit vector aligned with the vertical axis of the tower, respectively.

Fig. 14 shows the power spectrum of M_{yaw} for SRWT and DRWT in NBL and CBL flows. The five scatter points in Fig. 14 correspond to the dominant frequencies with the highest M_{yaw} strength for DRWT and SRWT. It is clearly shown that there is almost no difference in M_{yaw} strength and dominant frequencies between SRWT and the front rotor of DRWT in corresponding ABL flow. This is because the lateral asymmetry of the inflow wind causes M_{yaw}, and the back rotor has little effect on this phenomenon. Due to the obstruction of the front rotor of DRWT to the wind inflow, the M_{yaw} of the back rotor is reduced in both NBL and CBL flows. The power spectrum of M_{yaw} for both SRWT and the front rotor of DRWT have peaks at the position of the "Blade passage frequency" ($St = 6.69$), because NREL 5 MW wind turbine contains three blades, and every 1/3 rotation period there will be a clear lateral asymmetry between the right and left side of the disk. This feature was captured by other scholars in related studies (Churchfield et al., 2012; Ning and Wan, 2019; Lee et al., 2013).

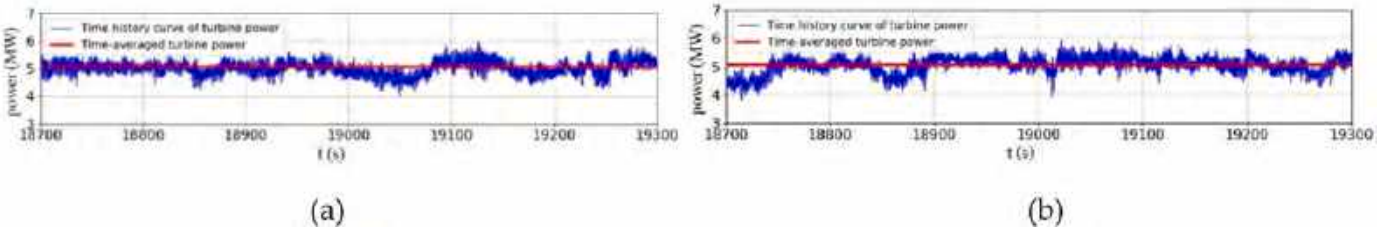

Fig. 10. Time variation and time-averaged value of turbine power output under ABL. (a) NBL; (b) CBL.

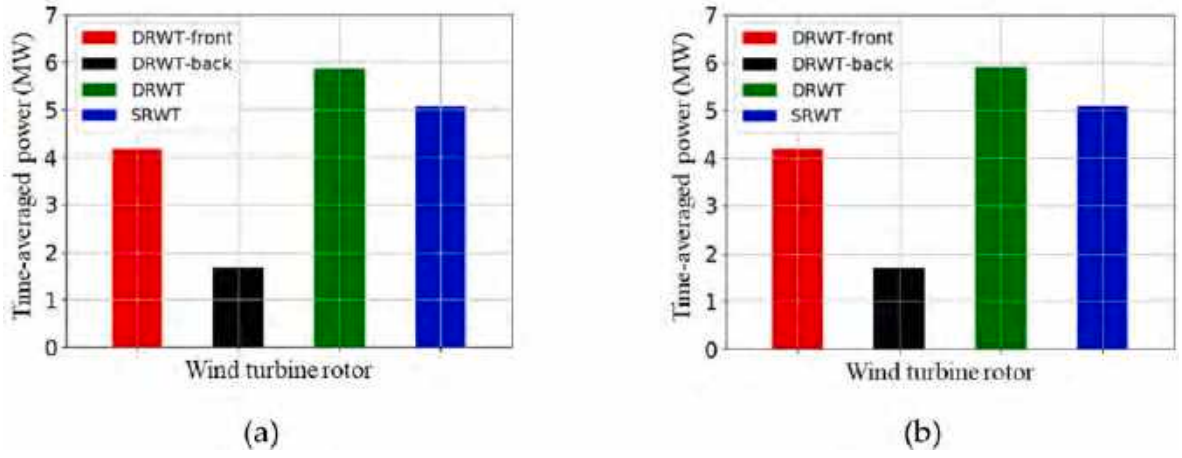

Fig. 11. Time-averaged power production of a single wind turbine under ABL. (a) NBL; (b) CBL.

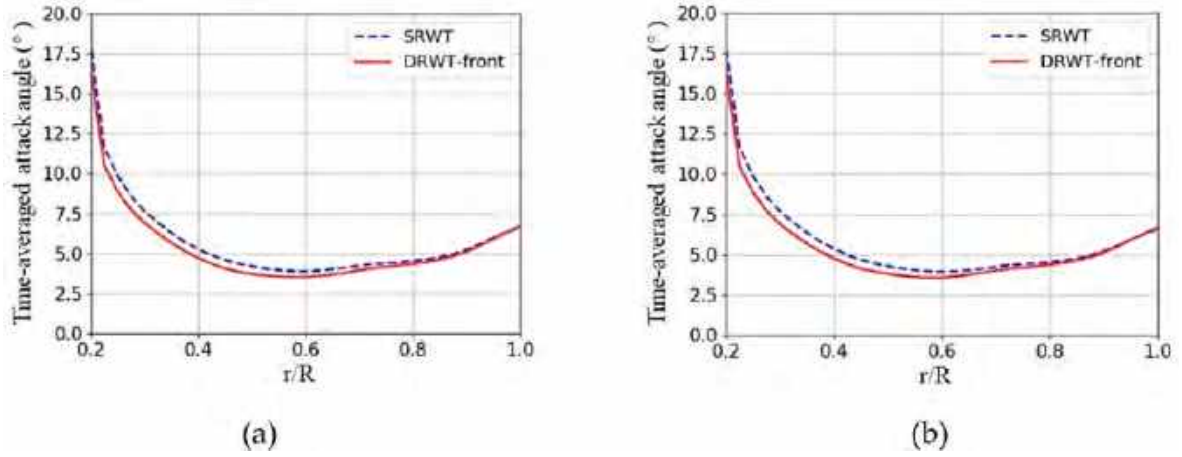

Fig. 12. Time-averaged attack angle profiles of SRWT and the front-rotor of DRWT along the radial direction under ABL. (a) NBL; (b) CBL.

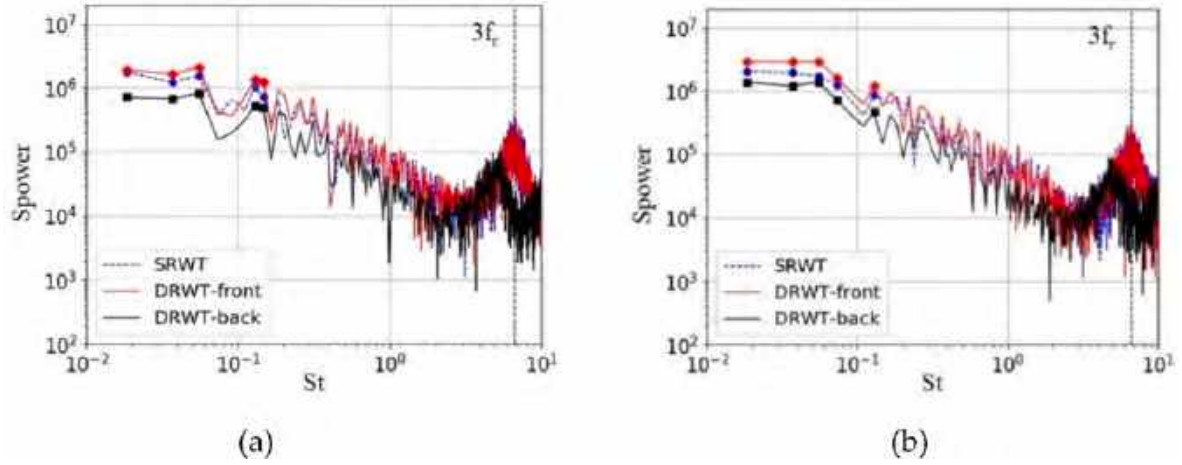

Fig. 13. Spectrum of power output for SRWT and DRWT under ABL. (a) NBL; (b) CBL.

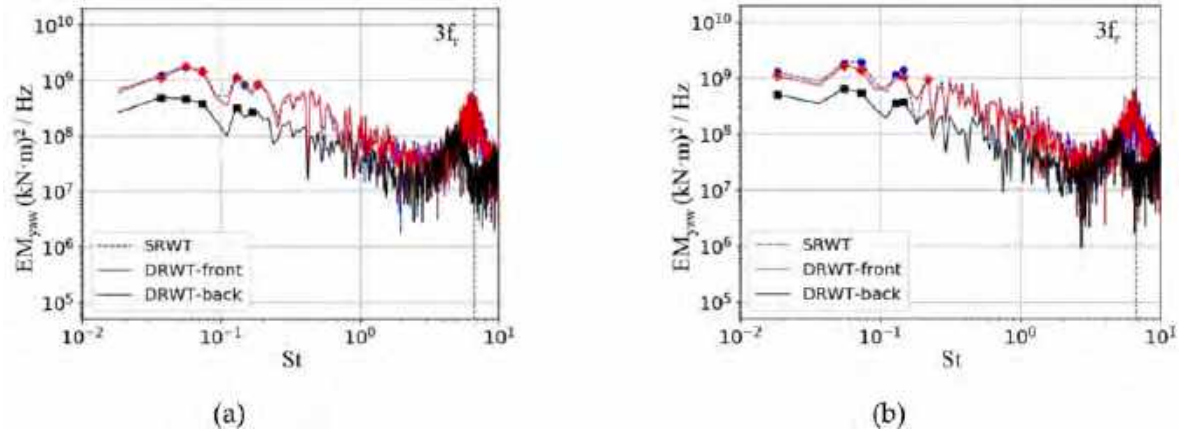

Fig. 14. Power spectrum of M_{yaw} for SRWT and DRWT under ABL. (a) NBL; (b) CBL.

The power spectrum of M_{oop} for SRWT and DRWT under NBL and CBL are plotted in Fig. 15. In the low frequency region, the dominant frequencies of M_{oop} for SRWT and the front rotor of DRWT are different and irregular, and the strength of M_{oop} for the front rotor of DRWT is higher compared with that of SRWT in both NBL and CBL flows in this region. The reason is that M_{oop} is associated with only one blade of the turbine, it is more sensitive to external disturbance. Different from M_{yaw}, the power spectrum of M_{oop} have peaks at the position of the "Rotor revolution frequency" ($St = 2.23$), and its frequency doubling, and the peaks are higher in the case of NBL due to the greater velocity gradient along the height direction.

3.2.3. Analysis of wake characteristics

The structure of DRWT is obviously different from that of SRWT, thus

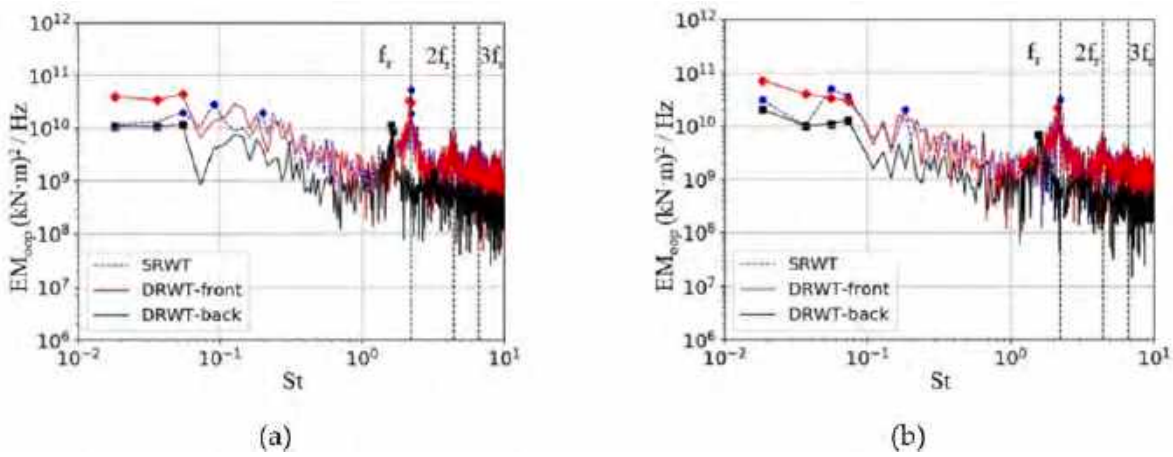

Fig. 15. Power spectrum of M_{oop} for SRWT and DRWT under ABL. (a) NBL; (b) CBL.

the wake characteristics will be quite different. In this part, we analyze the wake characteristics of DRWT in NBL and CBL flows, and in comparison to that of SRWT.

Time-averaged wake velocity deficit contours for the SRWT and the DRWT at hub height in NBL and CBL flows are presented in Fig. 16, and the wake velocity deficit is calculated as:

$$U_d = \frac{U_{in} - U_{wake}}{U_{in}} \tag{16}$$

where U_{in} and U_{wake} represent the inflow wind speed and wake speed, respectively.

Note that, in this work, we do not calculate the tower and the nacelle of the wind turbine, so a high-speed tube behind the turbine rotor can be found. As the wind turbine absorbs the incoming wind flow energy, there will be a significant velocity deficit behind the turbine, and the black solid lines denote the velocity deficit profile at different downstream locations. Furthermore, a faster wake velocity deficit recovery and a greater wake width can be found in CBL cases, which is in agreement with the work of Ning et al. (Ning and Wan, 2019).

DRWT has a larger wake velocity deficit near the rotor compare with that of SRWT, however, the wake velocity deficit recovery for DRWT is faster. Fig. 17 draws the contours of the wake velocity deficit for the DRWT minus that of the SRWT in y'-z plane at different downstream locations in NBL and CBL flows. The rotor center and boundary are marked by "+" and black circle. It is obviously shown that the wake velocity deficit of the DRWT is larger than that of the SRWT in the range of 4D-6D behind the turbine, while in the range of 7D-9D, they relatively close to each other, and this phenomenon is more obvious in CBL flow. The above result can be explained from two perspectives: the difference of ABL characteristics and the effect of the type of wind turbine.

The vortices will shed from the root and tip of the rotor and move downstream with the wake during the operation of wind turbine. The tip vortices are in the strong shear area between incoming ABL flow and the wake, and thus prone to unstable and breakdown. However, this phenomenon is not obvious in the near wake region, thus the tip vortices hinder the interaction between the incoming ABL flow and the wake in this region (Lignarolo et al., 2013). The time-averaged vorticity magnitude field for the SRWT at hub height in NBL and CBL flows are shown in Fig. 18, and it is shown that the tip vortices breakdown is advanced in CBL case compared with that of NBL case due to stronger unstable atmospheric disturbance. Therefore, in CBL case, the interaction between the wake and incoming ABL flow is advanced and strengthened, which accelerates the wake velocity deficit recovery.

The time-averaged vorticity magnitude field for the DRWT at hub height in NBL and CBL flows are shown in Fig. 19. The tip vortices will shed from both the front rotor and the back rotor of the DRWT, thus leading to a larger vorticity magnitude behind the DRWT compared with that of the SRWT. However, when comparing Figs. 18(a) and Fig. 19(a), it can be found that the tip vortices for both the SRWT and the DRWT obviously breakdown at about 3D downstream of the turbine in NBL flow, but the vorticity magnitude change of the DRWT is larger (decreasing from a large value in the DRWT case to a small value similar to the SRWT case). Meanwhile, this tendency also occurs in the CBL case at about 2D downstream of the rotor (comparing Figs. 18(b) and Fig. 19

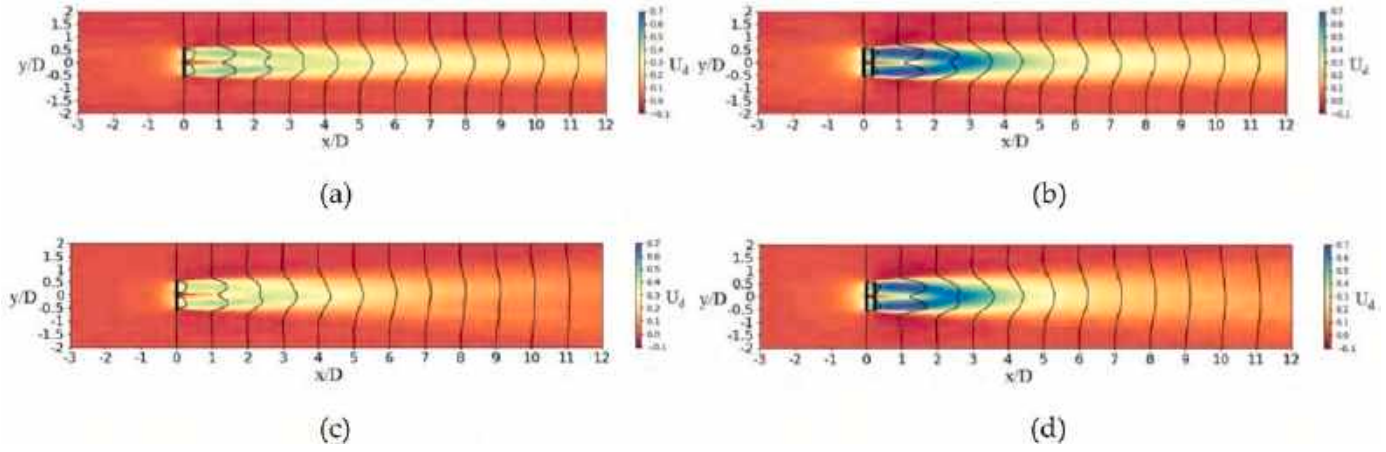

Fig. 16. Time-averaged wake velocity deficit contours at hub height. (a) SRWT under NBL; (b) DRWT under NBL; (c) SRWT under CBL; (d) DRWT under CBL.

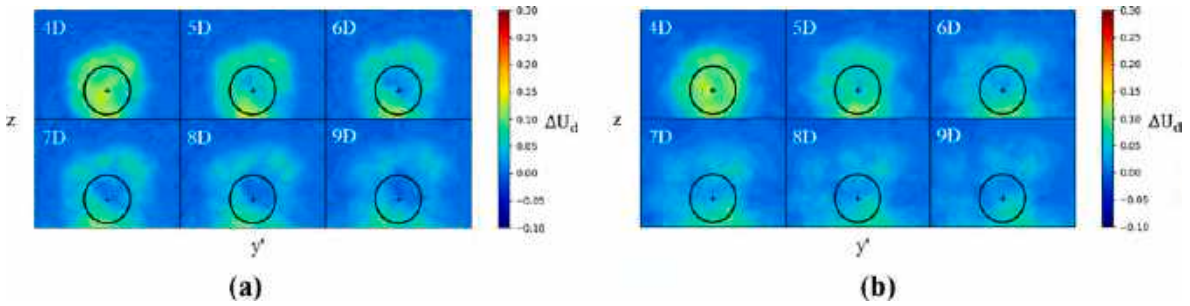

Fig. 17. The wake velocity deficit contours for DRWT minus that of SRWT in y'-z plane at different downstream locations under ABL. (a) NBL; (b) CBL.

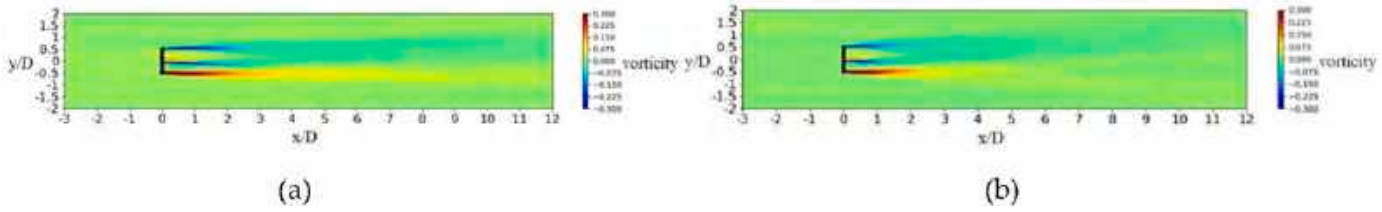

Fig. 18. Time-averaged vorticity magnitude field for SRWT at hub height under ABL. (a) NBL; (b) CBL.

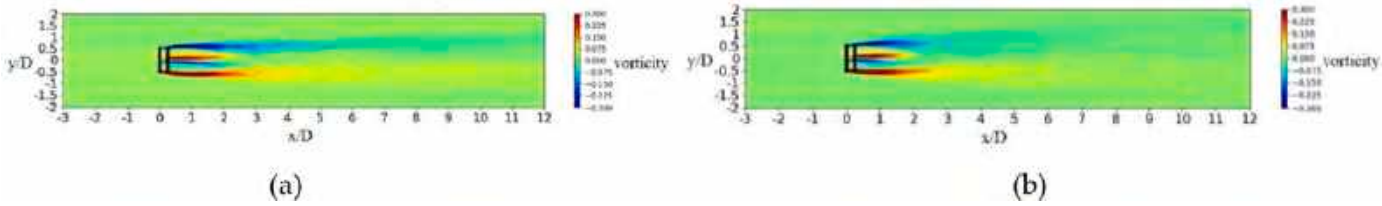

Fig. 19. Time-averaged vorticity magnitude field for DRWT at hub height under ABL. (a) NBL; (b) CBL.

(b)), which means that there are large differences in the wake boundary area between the DRWT and the SRWT.

Kaushik et al. (2017) stated that the streamwise fluctuation velocity is the main contributor for the turbulence disturbance in the wake area of turbine. Hence, the average power spectrum of streamwise fluctuation velocity of 24 uniformly arranged points on the rotor edge in the cross section of 2D, 4D, 6D and 8D downstream of the DRWT and the SRWT in both NBL and CBL flows are respectively plotted in Figs. 20 and 21. The power spectrum density in y-axis is nondimensionalized by $Su'/(Du_{hub})$ and the black solid line denotes "-5/3 power law".

As shown in Fig. 20, in NBL case, the strength of streamwise fluctuation velocity at the rotor edge for the DRWT in the near wake region (2D) is obviously higher than that of the SRWT, indicating that the flow at the wake boundary region for the DRWT is more complicated than that of the SRWT. When the downstream spacing increases from 2D to 4D, the strength of streamwise fluctuation velocity in low-frequency region decreases while in the high-frequency region increases, reflecting the energy transfer from the low-frequency large-scale turbulence to the high-frequency small-scale turbulence. As the downstream spacing reaches 6D, the strength of streamwise fluctuation velocity of both the DRWT and the SRWT on the rotor edge decrease in the frequency domain, indicating that the large-scale turbulence energy is still transferred to the small-scale turbulence, meanwhile, the small-scale turbulence starts to dissipate; the strength of streamwise fluctuation velocity for DRWT still higher than that of SRWT, but the difference between them decreases compared with that in 2D and 4D downstream of the turbine. As the downstream spacing increases to 8D, the difference in the strength of streamwise fluctuation velocity on the rotor edge between the DRWT and the SRWT is further reduced.

As shown in Fig. 21, in CBL case, the strength of streamwise fluctuation velocity on the rotor edge for the SRWT and the DRWT in low-frequency region is higher than that of the NBL case due to the higher low-frequency large-scale turbulent energy under CBL; besides, the strength of streamwise fluctuation velocity of the DRWT is higher than that of the SRWT, and it is the same as the NBL case. The strength of streamwise fluctuation velocity on the rotor edge undergoes a similar variation to that of the NBL case as the downstream spacing increases.

Calaf et al. (2010) and Allaert et al. (Allaerts and Meyers, 2015) noted that the momentum transport between the incoming ABL flow and the wake is primarily provided by the Reynolds stress, and it is a key point in determining the speed of wake velocity deficit recovery. Subsequently, Moghadassian et al. (2016) extended it to the radial value of Reynolds stress ($\overline{u_r' u_x'}$), and we referred to their ideas and plotted the dimensionless Radial Reynolds stress ($\overline{u_r' u_x'}/\overline{u_{hub}}^2$) for the DRWT and the SRWT (Case 1 to Case 4) at hub height under CBL and NBL in Fig. 22.

It is clearly found that the dimensionless Radial Reynolds stress in the wake area of the DRWT under CBL is the largest in the above cases, indicating that more momentum exchange between the free incoming ABL flow and the wake in this case, which corresponds well to the results in the preceding text.

Wake meandering is a common phenomenon appears after the full development wake flow of the wind turbine under ABL (Naumov et al., 2014), which makes the downstream wind turbines dynamically influenced by the wake of the upstream wind turbine, thus the aerodynamic loads of the downstream wind turbines is affected. Some studies were conducted in response to the wake meandering (Ning and Wan, 2019; Foti et al., 2016, 2018a, 2018b), however, limited to SRWT. Thus, we perform a relatively simple analysis of the wake meandering behind DRWT in ABL flow.

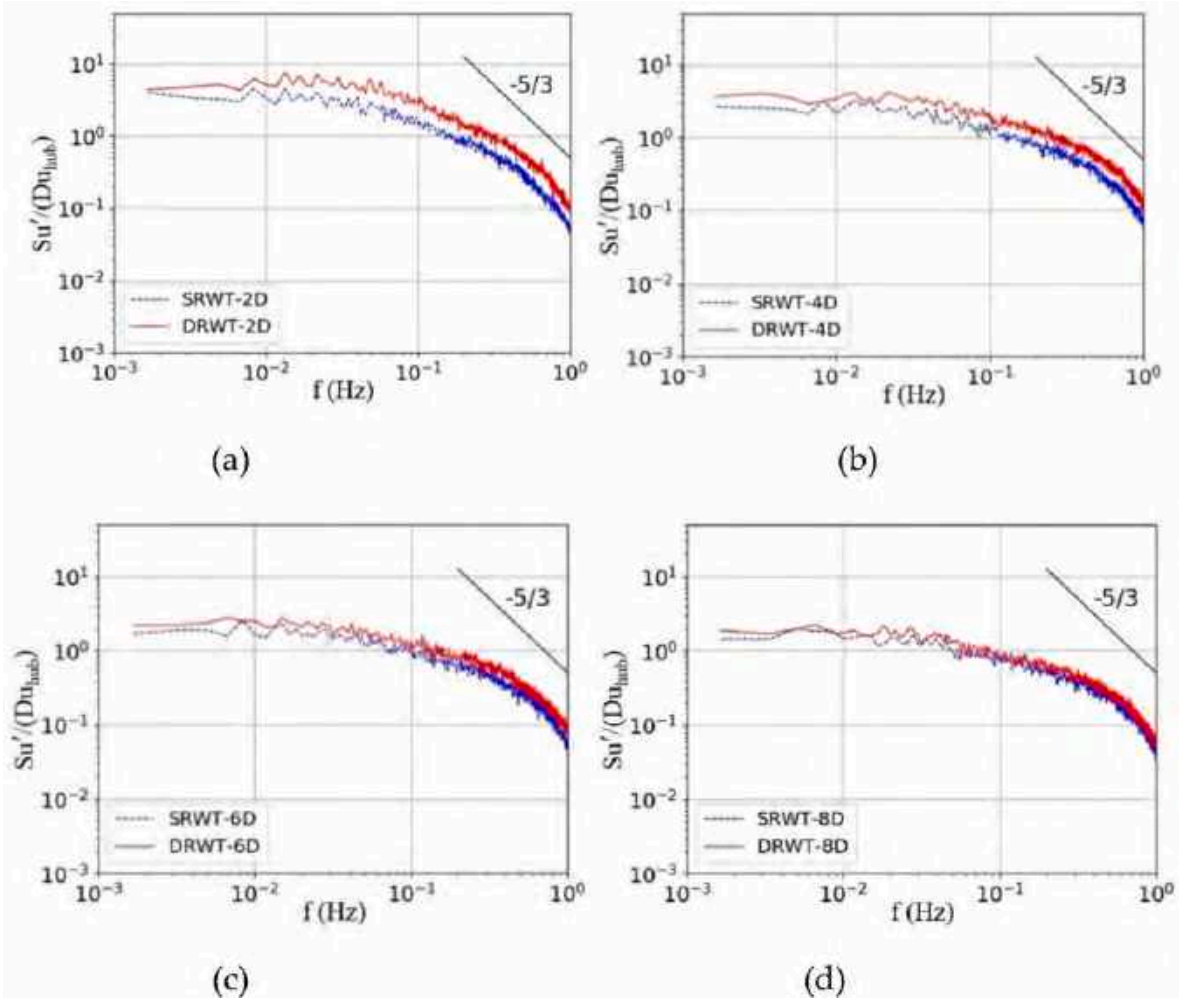

Fig. 20. Power spectrum of streamwise fluctuation velocity at the rotor edge in the cross section of different downstream positions under NBL. (a) 2D; (b) 4D; (c) 6D; (d) 8D.

Foti et al. (2016) pointed out that large-scale wake meandering profiles can be visualized more accurately by temporally filtering the instantaneous flow fields. Meanwhile, Ning et al. (Ning and Wan, 2019) also used this method to studied wake meandering in NBL and CBL flows. In this work, we referenced to their ideas and parameter settings, and plotted the temporally filtered velocity deficit contours of the DRWT under two kinds of ABL as shown in Fig. 23. It is clearly shown that the wake wiggles in both vertical and horizontal directions. The black solid line represents the wake center corresponds to a Gaussian fit to the wake velocity deficit at downstream positions, and the black dash line is the wake boundary ($\mu \pm 2\sqrt{ln\,2}\sigma$) based on Gaussian fitting result (Qian and Ishihara, 2018). It is obviously shown that the wake velocity deficit of the DRWT conforms to the Gaussian distribution, which is the same as SRWT.

Following the idea of Ning et al. (Ning and Wan, 2019), we plotted the root mean square (RMS) of the wake deflection for DRWT and SRWT to represent the wake meandering amplitude from 4D to 9D downstream positions as shown in Fig. 24, and it is calculated as:

$$\delta_{rms}(x) = \sqrt{\overline{\delta(x,t)^2}}, \delta_v = \mu_v - z_{hub}, \delta_h = \mu_h \tag{17}$$

where δ_v and δ_h are the wake deflection value in vertical and horizontal directions, respectively. δ_{rms} in y-axis is nondimensionalized by δ_{rms}/R, in which R=63m denotes the rotor radius.

It is shown that the wake deflection amplitude in vertical direction is lower than that in horizontal direction for either the DRWT or the SRWT in ABL flow due to the presence of the ground, which is consistent with the conclusion of Ning et al. (Ning and Wan, 2019). In NBL case, the horizontal wake deflection amplitude of the DRWT is higher than that of the SRWT from 4D to 7D due to the more complex wake characteristics in the wake boundary region of the DRWT; however, as the tandem spacing increases, the difference of horizontal wake deflection between the DRWT and the SRWT obviously decreases. Similar trends exist in the vertical wake deflection, but the difference between the DRWT and the SRWT is small. Nevertheless, in CBL case, both horizontal and vertical wake deflections of the DRWT are higher than that of the SRWT from 4D to 9D downstream behind the rotor.

3.3. Aerodynamic performance of downstream wind turbines under ABL

According to the previous results analyzed in section 3.2.3, there are obvious differences between the wake characteristics for the DRWT and the SRWT, and it can be expected that the aerodynamic performance of downstream turbines will be affected. In this part, the effects of the DRWT on the power production and aerodynamic moments of downstream turbines with different tandem spacings under ABL are analyzed, and the results are compared with the cases that the SRWT is located at the first row. The locations of wind turbines and numerical simulation cases are shown in Fig. 5 and Table 1.

3.3.1. Analysis of power production

Fig. 25 draws the time-averaged power production of each turbine

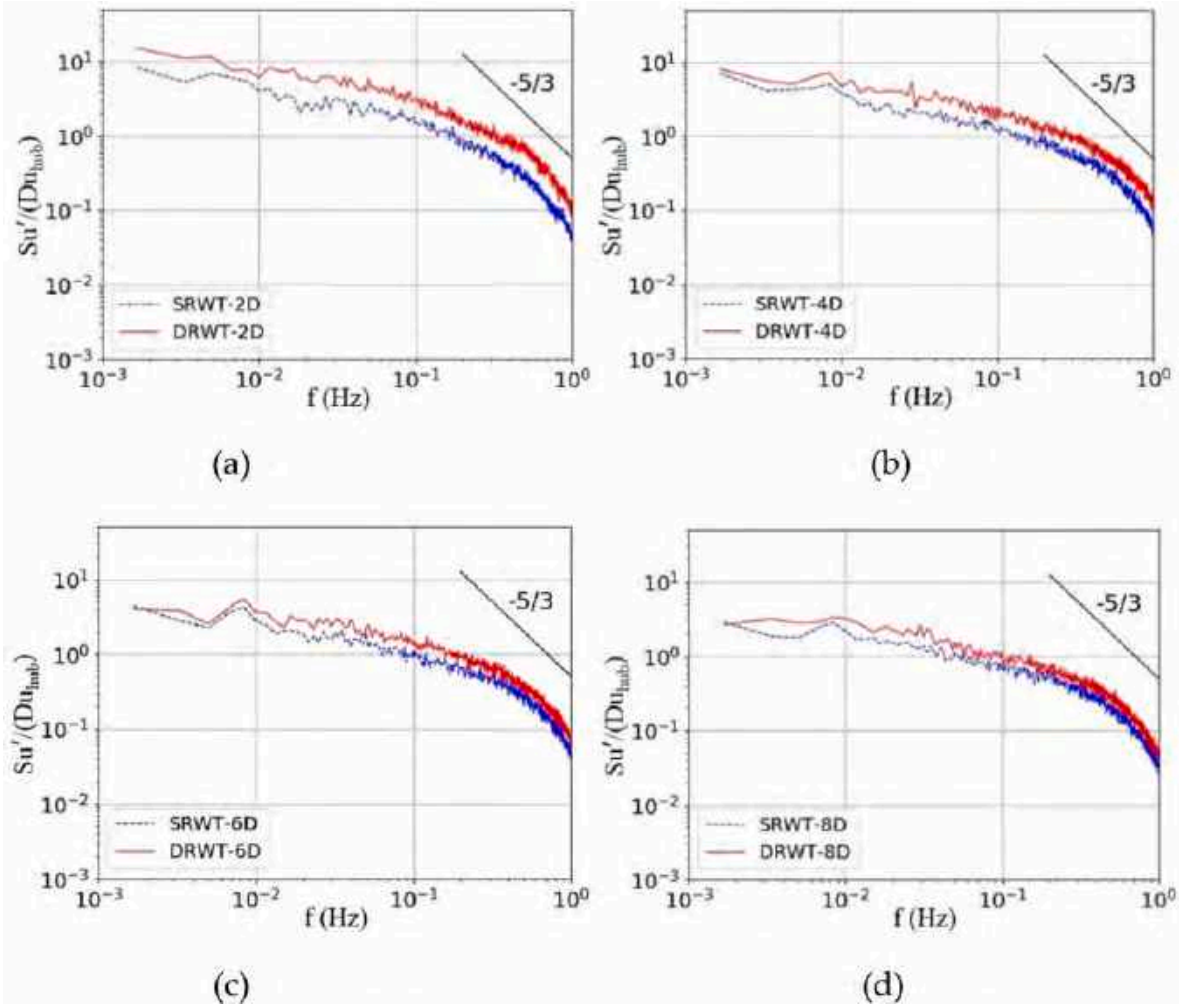

Fig. 21. Power spectrum of streamwise fluctuation velocity at the rotor edge in the cross section of different downstream positions under CBL. (a) 2D; (b) 4D; (c) 6D; (d) 8D.

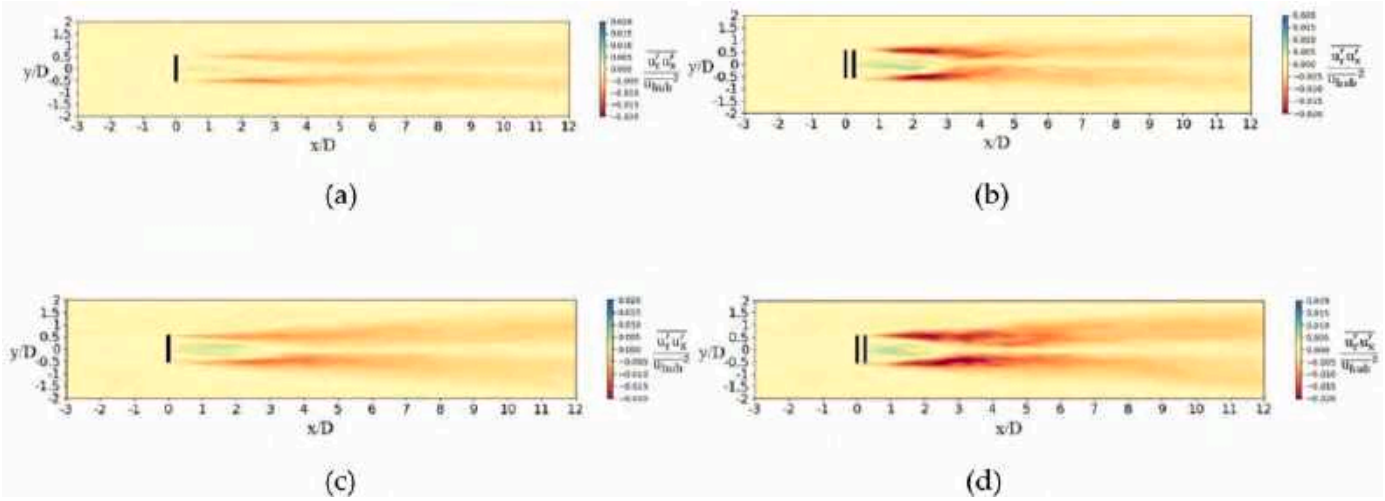

Fig. 22. Dimensionless Radial Reynolds stress contours at hub height under ABL. (a) SRWT in NBL flow; (b) DRWT in NBL flow; (c) SRWT in CBL flow; (b) DRWT in CBL flow.

from case 5 to case 16. Here, the power production is normalized by the time-averaged power of the SRWT located in the first row in the corresponding ABL flow.

It is obviously found that the time-averaged power production of downstream turbines located behind both the SRWT and the DRWT increase with the increasing of longitudinal spacing owing to the wake

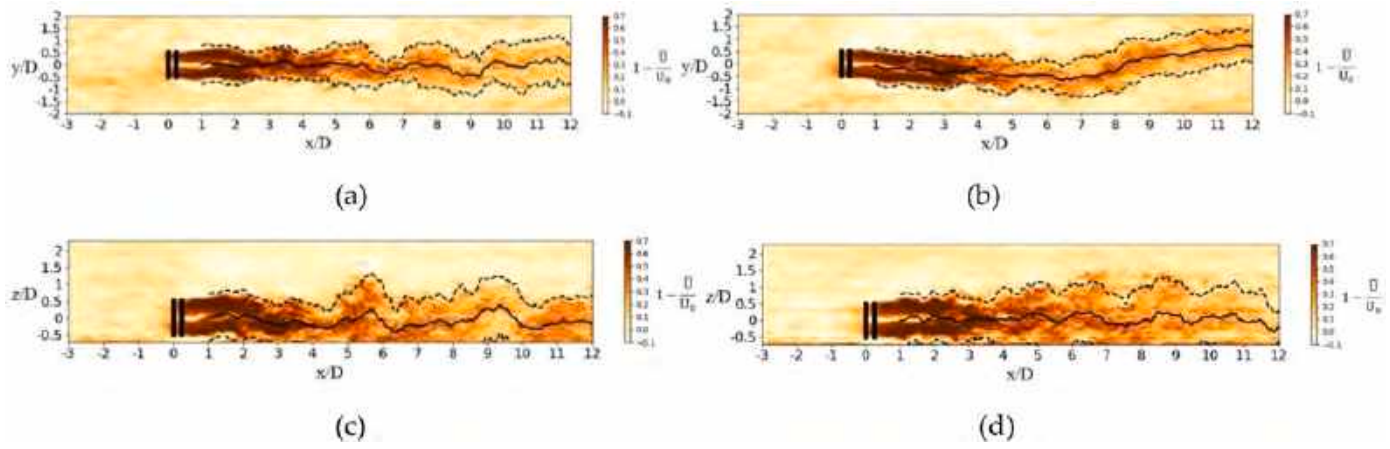

Fig. 23. Temporally filtered instantaneous velocity deficit contours of DRWT under ABL. (a) Hub height plane under NBL; (b) Hub height plane under CBL; (c) Central longitudinal plane under NBL; (d) Central longitudinal plane under CBL.

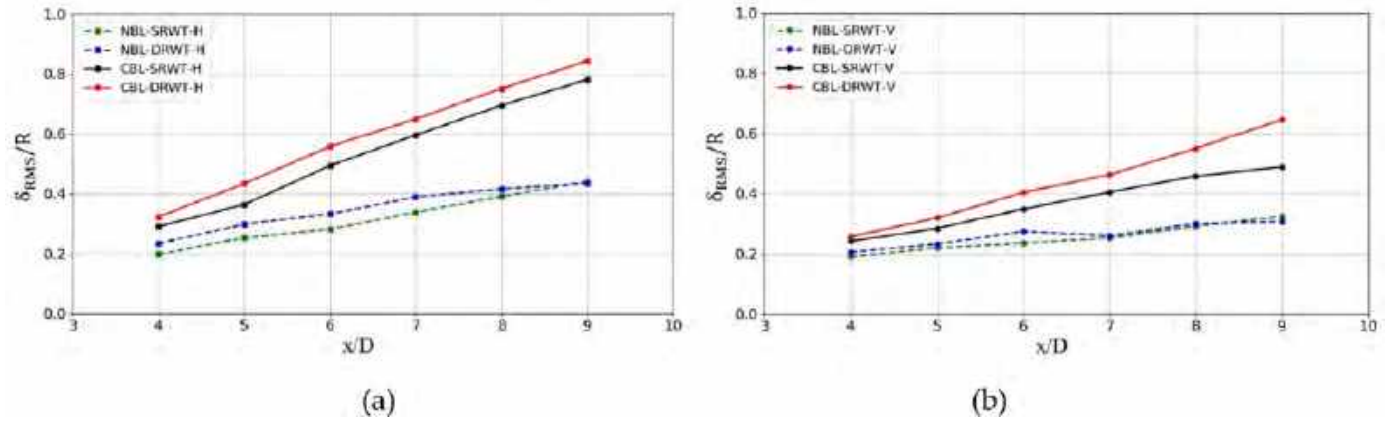

Fig. 24. Dimensionless RMS of wake deflection in horizontal and vertical directions for DRWT and SRWT under ABL. (a) Horizontal direction (b) Vertical direction.

velocity recovery; in the same wind turbine arrangement, for example, case 5 and case 7, the power production of downstream turbines is higher in CBL cases compared with NBL cases.

When the longitudinal spacing is 5D, the power production of the second-row turbine (WT2) located behind the DRWT is less than that located behind the SRWT in both NBL and CBL flows due to the larger wake velocity deficit demonstrated in Fig. 17. However, the power production of the third-row turbine (WT3) located behind the DRWT and that located behind the SRWT is nearly identical, and this is because the superposition of the low velocity wake of DRWT and the wake of WT2 enhances the momentum exchange behind WT2, thus accelerating the recovery of the wake velocity deficit behind WT2; taking NBL case as an example, the above analysis can be demonstrated by Fig. 26(a) and (b). As the longitudinal spacing reaches 7D, the power production of WT2 located behind the DRWT is still less than that located behind SRWT, however, the difference between them is less than the case of 5D owing to the faster wake velocity deficit recovery of DRWT, which has been explained in section 3.2.3; besides, the power production of WT3 located behind the DRWT is slightly lower than that located behind the SRWT, but the difference is almost negligible. When the longitudinal spacing reaches 9D, the difference between power production of WT2 located behind the DRWT and the SRWT is further reduced, and the power production of WT3 located behind the DRWT is almost identical to that located behind the SRWT.

Fig. 27 draws the total power production of three wind turbines under NBL and CBL. For the smaller tandem spacing arrangement (5D in this work), although the power output of WT2 located behind the DRWT is lower than that located behind the SRWT, the total power production of three wind turbines in DRWT cases are higher than that of SRWT cases, and this phenomenon is satisfied in both NBL and CBL flows. As the tandem spacing increases, the total time-averaged power production of three wind turbines in DRWT cases are also larger than that of SRWT cases, and the total power production increase from about 3.3% to 3% for the case of 5D tandem spacing to about 5.5% and 4.4% for the case of 9D tandem spacing in NBL and CBL flows, respectively.

3.3.2. *Analysis of aerodynamic moments*

The degree of dispersion of a set of data is mirrored by Standard deviation (STD), and a larger STD denotes a more severe fluctuation of the data. In this work, the M_{yaw} and M_{oop} of downstream turbines are analyzed. The STD value of M_{yaw} for downstream turbines in NBL and CBL flows are drawn in Fig. 28.

In NBL cases, when the longitudinal spacing is 5D, the STD value of M_{yaw} for WT2 located behind the DRWT is obviously higher than that located behind the SRWT. The reason for this phenomenon is that the wake behind the DRWT has a larger wake velocity deficit (as shown in Fig. 17) and a stronger wake meandering in the horizontal plane (as shown in Fig. 24) at a tandem spacing of 5D, leading to a stronger lateral asymmetry of the incoming flow in front of WT2 located behind the DRWT compared with that located behind the SRWT. The STD value of M_{yaw} for WT3 located behind the SRWT is higher than that of WT2 owing to the larger wake velocity deficit caused by the superposition of the wake from WT1 and WT2, which lead to a stronger lateral asymmetry of the incoming flow in front of WT3 compared with that of WT2; however,

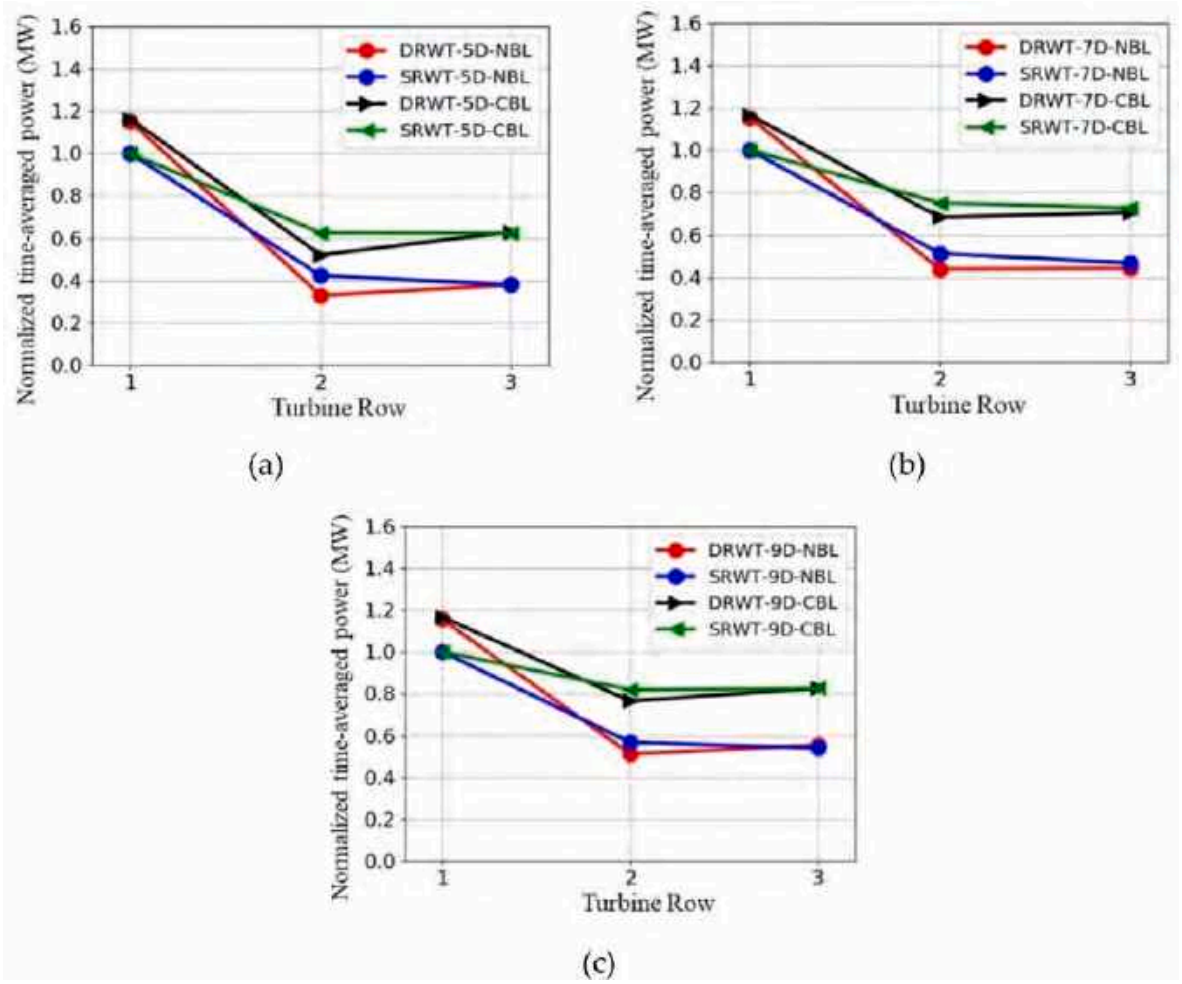

Fig. 25. Normalized time-averaged power production of different longitudinal spacings layout under ABL. (a) 5D; (b) 7D; (b) 9D.

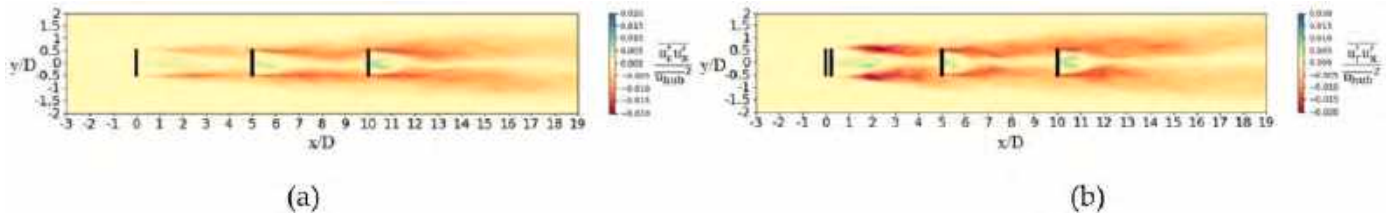

Fig. 26. Dimensionless Radial Reynolds stress contours at hub height under NBL. (a) SRWT-5D; (b) DRWT-5D.

the STD value of M_{yaw} for WT3 located behind the DRWT is lower than that of WT2, and this is because the inflow wind velocity in front of WT3 is significantly higher than that of WT2, which can be proved according to the result of power production in section 3.3.1, thus the lateral asymmetry of the incoming flow in front of WT3 is lower than that of WT2. As the longitudinal spacing reaches 7D, the STD value of M_{yaw} for WT2 located behind the DRWT is slightly higher than that located behind the SRWT, and the probable reason is that the incoming wind velocity in front of WT2 located behind the DRWT is slightly lower than that located behind the SRWT (as shown in Fig. 17) and the wake deflection in horizontal plane behind the DRWT is higher than that of the SRWT (as shown in Fig. 24); however, the difference between the STD value of M_{yaw} for WT2 located behind the DRWT and that located behind the SRWT is almost negligible. The STD value of M_{yaw} for WT3 located behind the SRWT is slightly higher than that of WT2 and the reason is similar to the case with a longitudinal spacing of 5D; besides, the STD value of M_{yaw} for WT3 located behind the DRWT is nearly identical to that of WT2 located behind the DRWT and slightly lower than WT3 located behind the SRWT. When the longitudinal spacing reaches 9D, the STD value of M_{yaw} for WT2 is nearly identical in both cases, meanwhile, the same phenomenon is also found in the results of WT3.

In CBL cases, the STD value of M_{yaw} for both WT2 and WT3 are significantly higher than those of NBL cases for all three longitudinal spacings owing to stronger atmospheric disturbance exacerbates the magnitude of wake deflection in the horizontal plane. The distribution trends of the STD value of M_{yaw} for WT2 and WT3 are almost similar to NBL cases at the corresponding tandem spacing and arrangement of turbines. Notably, the STD value of M_{yaw} for both WT2 and WT3 obviously decrease as the longitudinal spacing increases owing to the faster wake velocity recovery. However, this phenomenon does not appear in NBL flow.

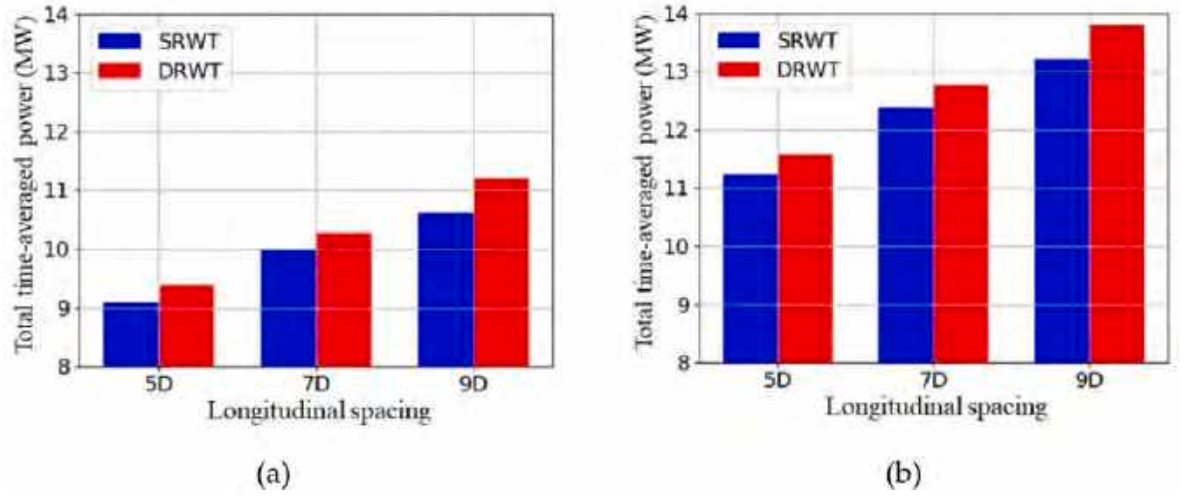

Fig. 27. Total time-averaged power production of three wind turbines under ABL. (a) NBL; (b) CBL.

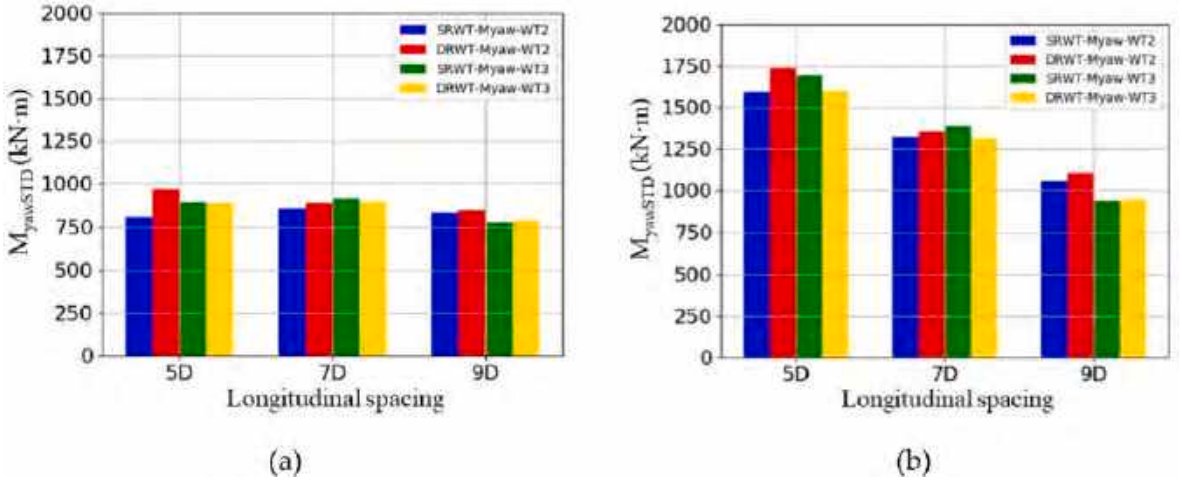

Fig. 28. STD values of M_{yaw} for downstream turbines under ABL. (a) NBL; (b) CBL.

Based on the above results, we can find that the stability of M_{yaw} for the WT2 located behind the DRWT is obviously deteriorated compared with that located behind the SRWT in both NBL or CBL cases when the longitudinal spacing is small (5D); however, the stability of M_{yaw} for WT3 located behind the DRWT does not deteriorate compared with that located behind the SRWT. As the longitudinal spacing increases (7D and 9D), there is no obvious deterioration in the stability of M_{yaw} for downstream turbines located behind the DRWT compared with that located behind the SRWT in both NBL and CBL cases.

Fig. 29 (a) and (b) shows the STD value of M_{oop} for downstream

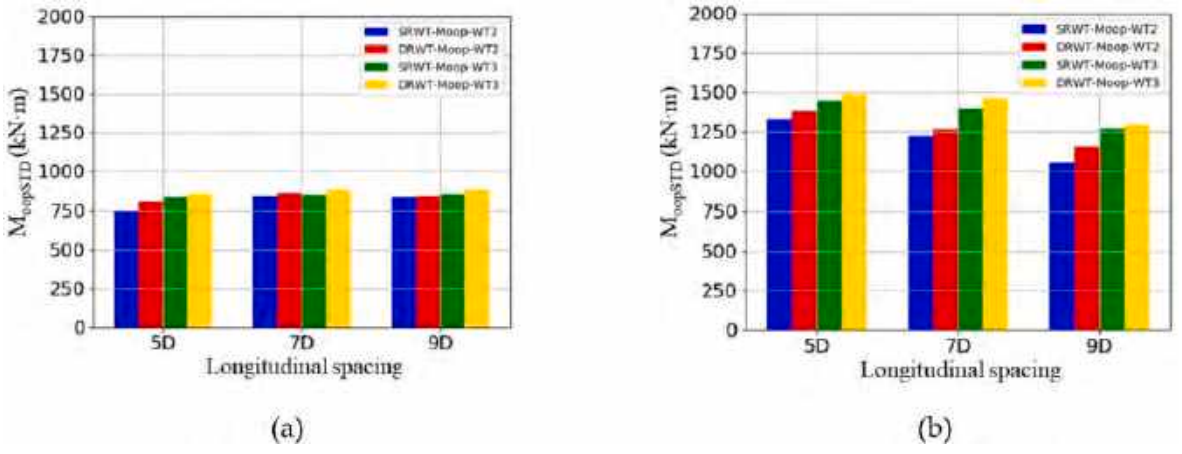

Fig. 29. STD values of M_{oop} for downstream turbines under ABL. (a) NBL; (b) CBL.

turbines in NBL and CBL flows, respectively.

In NBL cases, when the longitudinal spacing is 5D, the STD value of M_{oop} for WT2 located behind the DRWT is higher than that located behind the SRWT, and this is because DRWT has a higher wake velocity deficit and similar vertical wake deflection compared with SRWT at a downstream position of 5D, thus leading to a larger vertical asymmetry of incoming flow in front of WT2 located behind the DRWT. However, as the longitudinal spacing increases to 7D and 9D, the STD values of M_{oop} for WT2 located behind the DRWT and the SRWT are almost identical due to the similar wake velocity deficit and vertical wake deflection of the wake of DRWT and SRWT at the corresponding downstream positions. Notably, the STD value of M_{oop} for WT3 located behind the DRWT is slightly higher than those located behind SRWT at the corresponding tandem spacing, but this phenomenon is almost negligible.

In CBL cases, the STD values of M_{oop} for all downstream turbines gradually decrease as the longitudinal spacing increases owing to the faster wake velocity recovery, which shows a similar trend as the STD value of M_{yaw}, and this is markedly different to NBL cases. Furthermore, the STD values of M_{oop} for both WT2 and WT3 located behind the DRWT are higher than those located behind the SRWT in three tandem spacings (5D, 7D, 9D) used in this work.

Overall, for NBL cases, only the stability of M_{oop} for WT2 located behind the DRWT is decreased compared with that located behind SRWT when the longitudinal spacing is 5D, while the stability of WT3 located behind DRWT is not obviously deteriorated; as the longitudinal spacing increases (7D and 9D), the stability of M_{oop} for both WT2 and WT3 do not deteriorate compared with those located behind the SRWT. Nevertheless, for CBL cases, M_{oop} for both WT2 and WT3 located behind the DRWT are more unstable than those located behind the SRWT at all three longitudinal spacings.

4. Conclusions

In this work, the aerodynamic performance, wake characteristics of horizontal-axis DRWT and its effects on the downstream turbines are investigated in different atmospheric stabilities based on ALM and LES numerical methods. In the first part, the characteristics of two types of ABL and the accuracy of ALM are verified. Subsequently, the power production, aerodynamic moments, and wake characteristics of the SRWT and the DRWT are calculated and compared in NBL and CBL flows, and the effects of different ABL characteristics and wind turbine types on the results are analyzed. Finally, a tandem three wind turbines arrangement with a SRWT or DRWT placed in the first row are calculated under two types of ABL flows, and the aerodynamic loads of downstream turbines with different tandem spacings are compared and analyzed. The following conclusions are derived:

(1) The power production of the front rotor of DRWT is lower than that of SRWT in NBL and CBL flows owing to the disturbance of the back rotor of DRWT. Through spectrum analysis of power output, it is found that the dominant vibration frequencies of power output for the front rotor of DRWT are almost the same as those of the SRWT under two types of ABL flows, but the vibration amplitude of the front rotor of DRWT is higher.
(2) According to the power spectrum of aerodynamic moments, we find that the strength and dominant frequencies of M_{yaw} for the front rotor of DRWT are almost the same as those of the SRWT in both NBL and CBL flows. However, the strength and dominant frequencies of M_{oop} for the front rotor of DRWT is different from those of the SRWT.
(3) The wake velocity deficit recovery of DRWT is faster than SRWT, and this phenomenon is more obvious under CBL. The above results are due to the stronger disturbance of CBL and the difference in flow development between the DRWT and the SRWT around the wake boundary region. The wake velocity deficit of the DRWT satisfies the Gaussian distribution in both NBL and CBL flows, and based on this result, we find that both horizontal and vertical wake deflections of the DRWT are higher than those of SRWT in CBL flows. However, the difference in both horizontal and vertical wake deflections between DRWT and SRWT are slight at the far wake region in NBL flows.
(4) The power production of the WT2 located behind the DRWT is lower than that of the SRWT, while the difference between them decreases with increasing longitudinal spacing since DRWT has a faster recovery of wake velocity. For all three tandem spacings used in this work, the power production of WT3 located behind the DRWT is almost the same as that of the SRWT and the total power production of three turbines in DRWT cases are higher than those of SRWT cases. Notably, the above results hold for both NBL and CBL flows.
(5) For NBL flow, the stability of both M_{yaw} and M_{oop} for WT2 located behind the DRWT are deteriorated compared with those located behind the SRWT at a small longitudinal spacing (5D in this work) due to the larger wake velocity deficit of the DRWT, while the stability of both M_{yaw} and M_{oop} for WT3 located behind the DRWT do not deteriorate; as the tandem spacing increases (7D and 9D in this work), the stability of both M_{oop} and M_{yaw} for downstream turbines located behind the DRWT are not reduced compared with those located behind the SRWT. For CBL flow, due to the stronger atmospheric disturbance, the stability of both M_{oop} and M_{yaw} for downstream turbines are lower than those of NBL cases; however, the result of all CBL cases increase with increasing tandem spacing due to the faster recovery of wake velocity, which is significantly different from the NBL cases. In a small longitudinal spacing, the trend of the results are almost the same as NBL cases. The stability of M_{yaw} for all downstream turbines located behind the DRWT is not obviously deteriorated in larger tandem spacing compared with that located behind SRWT, nevertheless, M_{oop} for all downstream turbines located behind the DRWT are more unstable than those located behind the SRWT for all tandem spacings used in this work.

The DRWT used in this work is relatively simple, we do not consider the blade deformation. In future works, we will introduce the blade deformation into the DRWT to study its aerodynamic performance under ABL. Besides, the structure and control system of DRWT can be further designed and developed to enhance its performance and decrease negative effects on downstream wind turbines. Moreover, replacing part of SRWTs located in the large wind farm with DRWTs while maintaining the cost as low as possible, and investigate the optimization of the number and layout position of DRWT in the large wind farm to maximize the power production will also be considered further.

Funding

National Natural Science Foundation of China (52131102).

CRediT authorship contribution statement

Heming Bai: Data curation, Writing – original draft, preparation, Visualization, Investigation, Software, Validation. **Nina Wang:** Discussion, Investigation, Software, Validation. **Decheng Wan:** Supervision, Conceptualization, Methodology, Investigation, Writing – review & editing.

Declaration of competing interest

The authors declare that they have no known competing financial interests or personal relationships that could have appeared to influence the work reported in this paper.

Data availability

Data will be made available on request.

Acknowledgments

This work is supported by National Natural Science Foundation of China (52131102), to which the authors are most grateful.

References

Abkar, M., Porté-Agel, F., 2015. Influence of atmospheric stability on wind-turbine wakes: a large-eddy simulation study. Phys. Fluids 27, 035104.
Ainslie, J.F., 1988. Calculating the flowfield in the wake of wind turbines. J. Wind Eng. Ind. Aerod. 27, 213–224.
Allaerts, D., Meyers, J., 2015. Large eddy simulation of a large wind-turbine array in a conventionally neutral atmospheric boundary layer. Phys. Fluids 27, 065108.
Archer, C.L., Vasel-Be-Hagh, A., 2019. Wake steering via yaw control in multi-turbine wind farms: recommendations based on large-eddy simulation. Sustain. Energy Technol. Assessments 33, 34–43.
Bastankhah, M., Porté-Agel, F., 2014. A new analytical model for wind-turbine wakes. Renew. Energy 70, 116–123.
Bastankhah, M., Porté-Agel, F., 2016. Experimental and theoretical study of wind turbine wakes in yawed conditions. J. Fluid Mech. 806, 506–541.
Calaf, M., Meneveau, C., Meyers, J., 2010. Large eddy simulation study of fully developed wind-turbine array boundary layers. Phys. Fluids 22, 015110.
Chamorro, L.P., Arndt, R.E.A., Sotiropoulos, F., 2011. Turbulent flow properties around a staggered wind farm. Bound.-Layer Meteor 141, 349–367.
Chamorro, L.P., Tobin, N., Arndt, R.E.A., Sotiropoulos, F., 2014. Variable-sized wind turbines are a possibility for wind farm optimization. Wind Energy 17, 1483–1494.
Chatterjee, T., Peet, Y., 2019. Exploring the benefits of vertically staggered wind farms: understanding the power generation mechanisms of turbines operating at different scales. Wind Energy 22, 283–301.
Chen, Y., Li, H., Jin, K., Song, Q., 2013. Wind farm layout optimization using genetic algorithm with different hub height wind turbines. Energy Convers. Manag. 70, 56–65.
Chen, Y., Li, H., Jin, K., Elkassabgi, Y., 2015. Investigating the possibility of using different hub height wind turbines in a wind farm. Int. J. Sustain. Energy 36, 142–150.
Churchfield, M., Lee, S.. NWTC design codes (SOWFA). http://wind.nrel.gov/designcodes/simulators/SOWFA 2013.
Churchfield, M.J., Lee, S., Michalakes, J., Moriarty, P.J., 2012. A numerical study of the effects of atmospheric and wake turbine dynamics. J. Turbul. 13, N14.
Dou, B., Guala, M., Lei, L., Zeng, P., 2019. Wake model for horizontal-axis wind and hydrokinetic turbines in yawed conditions. Appl. Energy 242, 1383–1395.
Emeis, S., 2018. Wind Energy Meteorology: Atmospheric Physics for Wind Power Generation. Springer, Berlin/Heidelberg, Germany.
Fleming, P.A., Gebraad, P., Lee, S., Wingerden, J.-W.V., Johnson, K., Churchfield, M., Michalakes, J., Spalart, P., Moriarty, P., 2014. Evaluating techniques for redirecting turbine wakes using SOWFA. Renew. Energy 70, 211–218.
Foti, D., Yang, X., Guala, M., Sotiropoulos, F., 2016. Wake meandering statistics of a model wind turbine: insights gained by large eddy simulations. Phys. Rev. Fluids 1, 044407.
Foti, D., Yang, X., Sotiropoulos, F., 2018a. Similarity of wake meandering for different wind turbine designs for different scales. J. Fluid Mech. 842, 5–25.
Foti, D., Yang, X.L., Campagnolo, F., Maniaci, D., Sotiropoulos, F., 2018b. On the wake meandering of a model wind turbine operating in two different regimes. Phys Rev Fluids 3.
Frandsen, S., Barthelmie, R., Pryor, S., Rathmann, O., Larsen, S., Højstrup, J., Thøgersen, M., 2006. Analytical modelling of wind speed deficit in large offshore wind farms. Wind Energy Int. J. Prog. Appl. Wind Power Convers. Technol. 9, 39–53.
Gonzalez, J.S., Payan, M.B., Santos, J.R., 2013. A new and efficient method for optimal design of large offshore wind power plants. IEEE Trans. Power Syst. 28, 3075–3084.
GWEC. GLOBAL, 2021. *WIND REPORT 2021*; Global Wind Energy Council (GWEC): Brussels, Belgium.
Hollands, E.O., He, C., Gan, L., 2020. A particle image velocimetry study of dual-rotor counter-rotating wind turbine near wake. J. Visual 23, 425–435.
Hou, P., Hu, W., Chen, C., Soltani, M., Chen, Z., 2016. Optimization of offshore wind farm layout in restricted zones. Energy 113, 487–496.
Howland, M.F., Bossuyt, J., Martínez-Tossas, L.A., Meyers, J., Meneveau, C., 2016. Wake structure in actuator disk models of wind turbines in yaw under uniform inflow conditions. J. Renew. Sustain. Energy 8, 251–265.
Jiménez, Á., Crespo, A., Migoya, E., 2009. Application of a LES technique to characterize the wake deflection of a wind turbine in yaw. Wind Energy 13, 559–572.
Jonkman, J., Butterfield, S., Musial, W., Scott, G., 2009. Definition of a 5-MW Reference Wind Turbine for Offshore System Development. National Renewable Energy Lab. (NREL), Golden, CO, USA. No. NREL/TP-500-38060.
Katic, I., Højstrup, J., Jensen, N.O., 1987. A simple model for cluster efficiency. In: European Wind Energy Association Conference and Exhibition. A. Raguzzi, Rome, Italy.
Kaushik, T., Chatterjee, T., Peet, Y., Calhoun, R., 2017. In: Large Eddy Simulation Analysis of Wake Characteristics of a Wind Turbine Operating in Yaw. 35th Wind Energy Symposium, Grapevine, Texas.
Larsen, G.C., 1988. A Simple Wake Calculation Procedure. Risø National Laboratory, Roskilde, Denmark.
Lee, H., Lee, D.J., 2019. Wake impact on aerodynamic characteristics of horizontal axis wind turbine under yawed flow conditions. Renew. Energy 136, 383–392.
Lee, S., Churchfield, M.J., Moriarty, P.J., Jonkman, J., Michalakes, J., 2013. A numerical study of atmospheric and wake turbulence impacts on wind turbine fatigue loadings. J Sol Energ-T ASME 135, 031001.
Lignarolo, L.E.M., Ragni, D., Krishnaswami, C., Chen, Q., Simao Ferreira, C.J., Van Bussel, G.J.W., 2013. In: Experimental Analysis of the Kinetic Energy Transport and Turbulence Production in the Wake of a Model Wind Turbine. ICOWES2013 Conference, Lyngby.
Lu, H., Porté-Agel, F., 2011. Large-eddy simulation of a very large wind farm in a stable atmospheric boundary layer. Phys. Fluids 23, 065101.
Marathe, N., Swift, A., Hirth, B., Walker, R., Schroeder, J., 2016. Characterizing power performance and wake of a wind turbine under yaw and blade pitch. Wind Energy 19, 963–978.
Moeng, C.H.A., 1984. Large-eddy-simulation model for the study of planetary boundary-layer turbulence. J. Atmos. Sci. 41, 2052–2062.
Moghadassian, B., Rosenberg, A., Hu, H., Sharma, A., 2015. In: Numerical Investigation of Aerodynamic Performance and Loads of a Novel Dual Rotor Wind Turbine. 33rd Wind Energy Symposium, Kissimmee, Florida.
Moghadassian, B., Rosenberg, A., Sharma, A., 2016. Numerical investigation of aerodynamic performance and loads of a novel dual rotor wind turbine. Energies 9, 571.
Naumov, I.V., Mikkelsen, R.F., Okulov, V.L., Sørensen, J.N., 2014. PIV and LDA measurements of the wake behind a wind turbine model. In: J. Phys. Conf. Ser, vol. 524, 01268.
Newman, B.G., 1986. Multiple actuator-disc theory for wind turbines. J. Wind Eng. Ind. Aerod. 24, 215–225.
Ning, X., Wan, D.C., 2019. LES study of wake meandering in different atmospheric stabilities and its effects on wind turbine aerodynamics. Sustainability 11, 6939.
Ozbay, A., Wei, T., Hui, H., 2014a. A Comparative Study of the Wake Characteristics behind a Single-Rotor Wind Turbine and Dual-Rotor Wind Turbines. 32nd. AIAA Applied Aerodynamics Conference, Atlanta, GA.
Ozbay, A., Wei, T., Hui, H., 2014b. An Experimental Investigation on the Aeromechanics and Near Wake Characteristics of Dual-Rotor Wind Turbines (DRWTs). 32nd ASME Wind Energy Symposium. National Harbor, Maryland.
Pookpunt, S., Ongsakul, W., 2013. Optimal placement of wind turbines within wind farm using binary particle swarm optimization with time-varying acceleration coefficients. Renew. Energy 55, 266–276.
Qian, G.W., Ishihara, T., 2018. A new analytical wake model for yawed wind turbines. Energies 11, 665.
Rehman, S., Ali, S., 2015. Wind farm layout design using modified particle swarm optimization algorithm. In: International Renewable Energy Congress. IEEE, pp. 1–6.
Sharma, V., Cortina, G., Margairaz, F., Parlange, M.B., Calaf, M., 2018. Evolution of flow characteristics through finite-sized wind farms and influence of turbine arrangement. Renew. Energy 115, 1196–1208.
Sørensen, J.N., Shen, W.Z., 2002. Numerical modeling of wind turbine wakes. J. Fluid Eng. 124, 393–399.
Tian, L.L., Song, Y.L., Zhao, N., Shen, W.Z., Wang, T.G., 2020. Numerical investigations into the idealized diurnal cycle of atmospheric boundary layer and its impact on wind turbine's power performance. Renew. Energy 145, 419–427.
Troldborg, N., Sørensen, J.N., Mikkelsen, R.F., 2009. Actuator Line Modeling of Wind Turbine Wakes. Ph.D. Thesis. Technical University of Denmark, Lyngby, Danmark.
Turner, S.D.O., Romero, D.A., Zhang, P.Y., Amon, C.H., Chan, T.C.Y., 2014. A new mathematical programming approach to optimize wind farm layouts. Renew. Energy 63, 674–680.
Uemura, Y., Tanabe, Y., Mamori, H., Fukushima, N., Yamamoto, M., 2017. Wake deflection in long distance from a yawed wind turbine. J. Energ. Resour.-ASME 139, 051212.
Vasel-Be-Hagh, A., Archer, C.L., 2017a. Wind farm hub height optimization. Appl. Energy 195, 905–921.
Vasel-Be-Hagh, A., Archer, C.L., 2017b. Wind farms with counter-rotating wind turbines. Sustain. Energy Technol. Assessments 24, 19–30.
Veisi, A.A., Shafiei Mayam, M.H., 2017. Effects of blade rotation direction in the wake region of two in-line turbines using Large Eddy Simulation. Appl. Energy 197, 375–392.
Vested, M.H., Hamilton, N., Sørensen, J.N., Cal, R.B., 2014. Wake interaction and power production of variable height model wind farms. J. Phys. Conf. Ser. 524, 012169.
Wan, C., Wang, J., Yang, G., Gu, H., Zhang, X., 2012. Wind farm micro-siting by Gaussian particle swarm optimization with local search strategy. Renew. Energy 48, 276–286.
Wang, Z.Y., Ozbay, A., Tian, W., Hu, H., 2015. In: An Experimental Investigation on the Wake Characteristics behind a Novel Twin-Rotor Wind Turbine. 33rd Wind Energy Symposium, Kissimmee, Florida.
Wang, Z., Tian, W., Ozbay, A., Sharma, A., Hu, H., 2016a. An experimental study on the aeromechanics and wake characteristics of a novel twin-rotor wind turbine in a turbulent boundary layer flow. Exp. Fluid 57, 150.
Wang, Z.Y., Tian, W., Hu, H., 2016b. An Experimental Study on the Wake Characteristics of Dual-Rotor Wind Turbines by Using a Stereoscopic PIV Technique. 34th AIAA Applied Aerodynamics Conference, Washington, D.C.
Wang, Z., Ozbay, A., Tian, W., Hu, H., 2018. An experimental study on the aerodynamic performances and wake characteristics of an innovative dual-rotor wind turbine. Energy 147, 94–109.
Wang, X., Ye, Z., Kang, S., Hu, H., 2019. Investigations on the unsteady aerodynamic characteristics of a horizontal-Axis wind turbine during dynamic yaw processes. Energies 12, 3124.

Wei, D.Z., Wang, N.N., Wan, D.C., 2021. Modelling yawed wind turbine wakes: extension of a Gaussian-based wake model. Energies 14, 4494.
Wu, Y.T., Liao, T.L., Chen, C.K., Lin, C.Y., Chen, P.W., 2019. Power output efficiency in large wind farms with different hub heights and configurations. Renew. Energy 132, 941–949.
Yuan, W., Tian, W., Ozbay, A., Hu, H., 2014. An experimental study on the effects of relative rotation direction on the wake interferences among tandem wind turbines. Sci. China Phys. Mech 57, 935–949.
Zhang, M., Arendshorst, M.G., Stevens, R., 2019. Large eddy simulations of the effect of vertical staggering in large wind farms. Wind Energy 22, 189–204.
Zheng, Z., Gao, Z.T., Li, D.S., Li, R.N., Ye, L., Hu, Q.H., Hu, W.R., 2018. Interaction between the atmospheric boundary layer and a stand-alone wind turbine in Gansu—Part II: numerical analysis. Sci. China Phys. Mech. 61, 1–10.
Zhong, H., Du, P., Tang, F., Wang, L., 2015. Lagrangian dynamic large-eddy simulation of wind turbine near wakes combined with an actuator line method. Appl. Energy 144, 224–233.